FLOODED TWO-PHASE FLOW DYNAMICS AND HEAT TRANSFER WITH ENGINEERED WETTABILITY ON MICROSTRUCTURED SURFACES

A Thesis Presented to the Faculty of the Graduate School

at the University of Missouri-Columbia

In Partial Fulfillment

of the Requirements for the Degree

Master of Science

---

by

BO CHEN

Dr. Chung-Lung Chen, Thesis Supervisor

MAY 2015

The undersigned, appointed by the dean of the Graduate School, have examined the thesis entitled

FLOODED TWO-PHASE FLOW DYNAMICS AND HEAT TRANSFER WITH ENGINEERED WETTABILITY ON MICROSTRUCTURED SURFACES

Presented by Bo Chen,

A candidate for the degree of Master of Science

And hereby certify that, in their opinion, it is worthy of acceptance.

Professor Chung-Lung Chen

Professor Gary Solbrekken

Professor Carmen Chicone

ACKNOWLEDGEMENTS

I would like to express my profound gratitude and deep regards to my advisor, Dr. Chen, for his continuous support for my project, from initial advice in the early stages of conceptual inception to the warm encouragement to this day. He is a perfect teacher when I ask him for professional knowledge, while he is a lot like my father when we talk about career, life and future.

A special thank of mine goes to postdoc Sean and Simon for their valuable and constructive suggestions during the research. Sean gave me lots of suggestion and discussed with me on the numerical simulation and modeling. Simon advised me on the writing of papers and thesis, as well as rendering me some deep discussions related to my project.

I'm grateful to my friends Jingwen, Chenxing, Tiancheng and Steve who helped me a lot in completing my project and motivated me to keep working on the challenging project.

I wish to thank my parents for their undivided support which inspired me.

TABLE OF CONTENTS

LIST OF ILLUSTRATIONS

LIST OF TABLES

NOMENCLATURE

A_p	Surface area of a particle (m^2)
C_l	Relaxation coefficient for liquid phase (s^{-1})
C_g	Relaxation coefficient for gas phase (s^{-1})
D_{sm}	Sauter Mean Diameter (m)
$D_{v,air}$	Mass diffusion coefficient between species of water vapor and air (m^2/s)
d_s	Surface diameter (m)
d_v	Volume diameter (m)
$\vec{J_i}$	Diffusion flux of species i (mol/m^2 s)
M	Molecular weight (kg/kmol)
m''	Mass flux (kg/m^2 s)
$\dot{m}$	Volumetric mass flux (kg/m^3 s)
n	Mole's number (mol)
$\vec{n}$	Surface normal of a cell
$\hat{n}$	Unit normal
$\hat{n}_w$	Unit vector normal to the wall
F_{vol}	Volume force (N)
$\vec{g}$	Gravitation acceleration (m/s^2)
h_{lg}	Latent heat between liquid and gas phases (J/kg)
k	Thermal conductivity (W/m K)
$\dot{m}_{l\to g}$	Volumetric mass transfer rate from liquid phase to gas phase (kg/m^3 s)
$\dot{m}_{g\to l}$	Volumetric mass transfer rate from gas phase to liquid phase (kg/m^3 s)
p	Pressure (Pa)
p_{g_lg}	Pressure near the liquid-gas interphase on the gas side (Pa)

p_{sat}	Saturation pressure (Pa)
Q	Volumetric heat source term (W/m^3)
$Q_{l\to g}$	Volumetric heat source term from liquid phase to gas phase (W/m^3)
$Q_{g\to l}$	Volumetric heat source term from gas phase to liquid phase (W/m^3)
R	Universal gas constant (J/mol K)
r_e	Radius of bubble at equilibrium state (m)
T	Temperature (K)
T_{g_lg}	Temperature near the liquid-gas interface on the gas side (K)
T_{lg}	Temperature on the liquid-gas interface (K)
T_{sat}	Saturation temperature (K)
t	Time (s)
$\hat{t}_w$	Unit vector tangential to the wall
V_p	Volume of a particle (m^3)
V_{cell}	Volume of a cell (m^3)
$\vec{v}$	Overall velocity vector (m/s)
v_l	Inverse of density of the liquid (m^3/kg)
v_g	Inverse of density of the gas (m^3/kg)
W	Work (J)
$Y_i{}^j$	Local mass fraction of species i for phase j

Greek Symbols

α	Volume fraction
β	An expression of the accommodation coefficient
ε	Accommodation coefficient

θ_w	Contact angle at the wall (degree)
κ_l	Curvature for the liquid phase (1/m)
κ_g	Curvature for the gas phase (1/m)
μ	Dynamic viscosity (Pa s)
ρ	Density (kg/m^3)
σ	Surface tension (N/m)

Abbreviations

CHF	Critical Heat Flux
CSF	Continuum Surface Force model
HTC	Heat Transfer Coefficient
SMD	Sauter Mean Diameter
VOF	Volume of Fluid method

FLOODED TWO-PHASE FLOW DYNAMICS AND HEAT TRANSFER WITH ENGINEERED WETTABILITY ON MICROSTRUCTURED SURFACES

Bo Chen

Dr. Chung-Lung Chen, Thesis Advisor

ABSTRACT

Due to excessive droplet feeding, a period of flooding occurs as part of a typical droplet based thermal management cycle. The conventional superhydrophilic surface, which is designed for thin film evaporation because of its highly wettable character, has a limited improvement on the thermal performance during the flooded condition. This paper investigates micro-structures which combine micro-pillars and four engineered wettability patterns to improve the heat dissipation rate during flooding. Using the transient, 3-D volume-of-fluid (VOF) model, the bubble behaviors of growth, coalescence, and departure are analyzed within different micro-structures and the effects of pillar height and wettability patterns on the thermal performance are discussed. The wettability gradient patched on the pillar's side is demonstrated to promote the bubble's upward movement due to the contact angle difference between the upper and lower interfaces. However, insufficient pulling force results in large bubbles being pinned at the pillar tops, which forms a vapor blanket, and consequently decreases the heat transfer coefficient. When only a patch of hydrophobic material is present on the pillar top, effective pulling forces can be developed to help bubbles in the lower level depart from the pillar forest, since bubble merging between them generates most of the power required to pull the bubbles to the surface. The simulation results, including heat source temperatures and heat transfer coefficients, indicate that a patch of hydrophobic material on the pillar top works best out of all of the cases studied.

Chapter 1 INTRODUCTION

1.1 Background

Microelectronics is the heart of any modern electronic product, from household electronic items, to large electronic management systems. However, over the past several decades, transistor development has followed Moore's Law, which is the observation that the number of transistors on integrated circuits doubles every two years. This has led to significantly risen of heat flux from power devices, approaching as high as 1kW/cm^2 [1]. If not properly managed, the high microprocessor temperature will deeply affect the performance of the microelectronic assembly, degrade the system reliability, or even cause catastrophic failure. Moreover, the device miniaturization and design complexity are causing non-uniform power distribution on the microprocessors, leading to "high flux hot spot" [2, 3]. The heat flux in these regions can have a value that is several times higher than the average heat flux on the chip, reaching values as high as 5kW/cm^2. Therefore, novel cooling technologies must be developed for efficient thermal management, especially the cooling approaches that can specifically handle the microscale, high flux hot spot.

Conventional heat dissipation methods for high heat flux electronic modules are natural, forced, and mixed convection with single phase working fluids. However, the only determinant of the cooling efficiency is the sensible heat of the coolant. Accordingly, a high flow rate of the coolant is required to maximize the effect, and this approach brings up the pumping power issues. The other method is phase change heat transfer method, which has been extensively investigated in the past two decades, such as direct liquid immersion cooling [4, 5], microchannel cooling [6, 7], jet impingement cooling [8, 9], spray cooling [9-14], and electro-wetting cooling [15-17].

These phase change cooling techniques, which involve boiling and thin film evaporation, can transfer huge amounts of heat per unit area due to the large amount of latent heat.

Liquid immersion cooling is a practice to submerge electronic components into a thermal conductive liquid [5, 18]. Since some hot spots are susceptible to electromagnetic interference, such as Central Processing Unit (CPU), the liquid must have sufficiently low electrical conductivity to avoid interfering with the normal operation of the transistors. For this reason, the dielectric liquid is preferred. However, the liquid may require either to be regularly refilled or sealed, which is inconvenient, makes it an uncommon way for cooling computers, while it is the routine method of cooling large power distribution components such as transformers.

The microchannel was introduced by Tuckerman and Pease in 1981 [19]. Since the heat transfer efficiency can be greatly increased by decreasing the passage size, which results in a larger surface-area-to-volume ratio, the microchannels are usually made as small as possible. Tuckerman and Pease tested their optimum sized michrochannel, and found that a heated device could dissipate heat flux as high as 790W/cm^2, with only a 71 °C temperature rise. However, the high power consumption of pumps and valves, and the increased pressure loss in the microchannel passages, as well as the micro fabrication challenge, attenuate the benefits of this great invention [15].

Droplet based thermal management, including spray cooling and electro-wetting cooling, enables precise droplet feeding to the designed area, and has the potential to create a more uniform temperature distribution. Kim [12] gave a review regarding the mechanism for spray cooling, and the effects of non-condensable gas, surface enhancement, spray inclination and gravity. Horacek et al. [13] measured wall heat

transfer during spray cooling. The length of the contact line was shown to correlate with wall heat flux rather than the surface wetted area. Yang et al. [11] suggested that heat flux of 1000 W/cm^2 can be achieved using water at low flow rates. Another spray cooling investigation, using ammonia, by Bostanci et al. [14] showed high Critical Heat Flux (CHF) with 1100 W/cm^2.

Cheng and Chen [15] demonstrated that electrowetting-on-dielectric can cool down the hot spot surface by more than 40 °C within 2 s. Another work [16] published by them reported that a hot spot with a heat flux of 27 W/cm^2 was rapidly cooled down by 30 °C. The theoretical and numerical results for digitized heat transfer investigated by Baird and Mohseni [17] revealed that the enhancement of the heat transfer coefficient was due to the internal circulation inside of the droplets. They also summarized that the digitized heat transfer has the capability for active, on-demand suppression of transient heating on hot spots.

Inadequate coolant feeding frequency by droplet-based thermal management methods can easily cause periodic flooding. A flooded regime was reported as a periodic scenario occurring in droplet-based thermal management in Hsieh and Shen's work [10, 20]. Due to the favorable superhydrophilic surface used for liquid spreading, micro-structures worked efficiently in the thin film and partial dryout regimes. For the flooded regime, Hsieh and Yao [10] claimed that negligible effect on heat transfer performance can be induced by highly wettable surface textures. The flooded regime, which occupies about 20% of the total evaporation time [20], comes with boiling phenomenon which may cause large surface heat flux and surface temperature oscillations. Thus the heat transfer performance in the flooded regime will undoubtedly affect the thermal performance of the entire cooling process. However,

boiling and evaporation phenomena during flooding were rarely mentioned in former studies.

Our group [21] has proposed a micro-structure, which combines micro-pillar and engineered wettability patterns, to investigate the thermal phenomena under flooded conditions and improve the heat dissipation rate. The work compared the proposed structure with the flat hydrophilic surface and wettability patterned flat surface, and found that bubbles formed on the flat surface can hardly generate vertical momentum, while the proposed bi-philic micro-pillar structure can guide bubbles upwards, enhance bubble departure rate, and reduce bubble sizes. Additionally, the smoothness and coherence of the bubble departure were enhanced.

Following our prior work, micro-structures with different pillar heights under a flooded condition are examined to define the effect of pillar geometry on the thermal performance. Four wettability patterns combined with the micro-pillar structure are studied to understand their capability on facilitating bubble departure and thereby enhancing the heat transfer performance. The bubble's force and energy analysis are presented to explain the bubble dynamics.

1.2 Literature Review

1.2.1 Effects of wettability patterning and micro-structure

Surface physicochemical properties, including micro-structure and wettability, play an important role in boiling heat transfer [22]. One common approach to increase Heat Transfer Coefficient (HTC) and Critical Heat Flux (CHF) is to modify the heating surface condition by micro-structure fabrications [23]: (1) Surface modification by increasing surface roughness. Such modification generally increases surface wettability, which causes an increased CHF through the enhanced liquid

spreading over the heated area. Another effect of the surface modification is to increase the number of microscale cavities, which serve as the starting sites for heterogeneous nucleation of liquid for bubble formation; (2) Increasing the effective heat transfer surface area by thermal fin effect with microfabricated pin-fin structures; (3) Employing wicking structures to promote the liquid supply to the heated area by capillary pumping, thereby delaying the dry out.

Chen at el. [23] reported the study on pool boiling of water on Cu/Si made nanowires. They observed significant enhancement of both critical heat flux and thermal conductance on nanowires compared with plain surface. The reported CHF was about 200W/cm^2 among the highest value of pool boiling heat transfer. The enhancement could be attributed to some unique properties of nanowires. First, a surface coated with nanowires can be superhydrophilic; Second, nanowire arrays contain many orders of magnitude of cavities and pores compared to other treated surfaces, thereby effectively increased the nucleation site density and surface roughness; Third, nanowire arrays may act as efficient wicking structures.

Shen et al. [20] investigated the heated droplet impingement hydrodynamics for a range of heating levels corresponding to droplet non-boiling and boiling conditions. Impingement was tested on three types of surfaces: polished silicon, nano-structured porous silicon, and gold layered polished silicon. The nano-structured surface resulted in a reduced equilibrium contact angle and a significant reduction in energy dissipation during the initial impact spreading. They also pointed out that there were four major stages identified during the total droplet evaporation process, which were impact, boiling, nearly constant diameter evaporation and dry-out period. The nearly constant diameter increased with heating for the nano-structured non-boiling and boiling cases compared with the polished surfaces.

Biporous media consisting of large clusters of small particles have been shown to increase the heat dissipation capacity due to the capillary suction generated by small pores inside the particle clusters [24]. Coso et al. [25] studied micro structures in which pores separated microscale pin fins and generated high capillary suction, while larger microchannels were used to reduce overall flow resistance. Their experimental data showed that heat fluxes of up to 119.6 (±4.2) W/cm^2 can be dissipated in predominantly evaporation heat transfer. For larger pores and deeper wicks (pore > 16μm and depth >145μm respectively), nucleate boiling regime was observed with high dryout heat fluxes up to 277.0 (±9.7) W/cm^2 for large heaters (~1cm^2). For small heaters of area 0.0625 cm^2, high heat flux of up to 733.1 (±103.4) W/cm^2 can be dissipated. The overall HTC was increased with a reduction in pore size and accompanying increase in surface area.

Since the influence of wettability on boiling is complex: hydrophobic zones promote nucleation, while the hydrophilicity enhance the CHF, researchers raised many wettability patterns combining both hydrophobic and hydrophilic coatings to improve the thermal performance.

Betz et al. [26] demonstrated that smooth and flat surfaces combining hydrophilic and hydrophobic patterns improve pool boiling performance. They characterized different networks combining hydrophilic and hydrophobic regions. Patterning of mixed hydrophilic and hydrophobic areas can improve the CHF and HTC of a plain hydrophilic surface by 65% and 100%, respectively. Especially, spaces with hydrophilic networks (patterned with hydrophobic islands) enhance both CHF and HTC, while surfaces with hydrophobic networks seem to only enhance the HTC and might even reduce the CHF.

In another of their work, Betz et al. [27] characterize pool boiling on surfaces with wettabilities varied from superhydrophobic to superhydrophilic. The measurement results showed that the largest HTC were reached not on surfaces with spatially uniform wettability, but on biphilic surfaces, which juxtaposed hydrophilic and hydrophobic regions. They manufactured and tested the superbiphilic surfaces, which showed exceptional performance in pool boiling, combing high CHF over 100W/cm^2 with HTC over 100 kW/m^{2}K. They developed an analytical model, which described how biphilic surfaces effectively manage the vapor and liquid transport, delaying critical heat flux and maximizing the HTC. Both the analytical modeling and the experiments showed that the superbiphilic surfaces outperform all other surfaces in the low superheat regime.

Wang et al. [22] compared bubble formation on the micropattern coated copper surfaces with the uniform superhydrophobic coating and bare copper surfaces. They revealed that the micropattern coated copper surfaces had low bubble formation temperature to 85 ℃ which was similar to the uniformly coated superhydrophobic surfaces, whereas that of the bare copper surface stuck to around 124 ℃ with considerable super heat. Moreover, the superhydrophobic micropatterns controlled the nucleation sites, bubble shapes and growth rates, and prevented formation of a continuous vapor film which was likely developed on a uniform hydrophobic coating.

1.2.2 **VOF and mass transfer model in phase change investigations**

The VOF model can model two or more immiscible fluids by solving a single set of momentum equations and tracking the volume fraction of each of the fluids throughout the domain. It is widely used for the prediction of jet breakup, the motion

of bubbles in a liquid, the motion of liquid after a dam break, and the steady or transient tracking of any liquid-gas interface.

Yang et al. [28] investigated the boiling flow of R141B in a horizontal coiled tube. A numerical simulation, using the VOF method and the corresponding experiments were conducted. The comparison indicated that the phase distribution in various cases predicted by the simulations were consistent with the phenomenon observed in the experiments. The flow velocity showed a strong dependence on the phase distribution. Yang et al pointed out that, in bubbly flow vapor phase flowed with liquid phase, with little velocity differences between two phases, whereas in stratified flow vapor phase flowed much faster than the liquid phase, caused significant wave of the phase interface.

Chen et al. [29] numerically simulated the vapor-venting process in 3D in a rectangular microchannel with a hydrophobic porous membrane bounded on one side for phase-seperation. The simulation was based on the VOF method, and showed the vapor-venting mechanism can effectively mitigate the vapor accumulation issue, reduce the pressure drop, and suppress the local dry-out inside the microchannel. The pressure surge was also observed in the vapor-venting channel. Their simulation provided some insight into the design and optimization of vapor-venting heat exchangers.

A numerical investigation on bubble behavior in subcooled flow boiling of water under the effect of additional inertial forces has been performed by Wei et al. [30] based on the VOF method. The simulations were carried out on upward water flow in a vertical, rectangular duct with single side heating surface. It was pointed out by them that the centrifugal force and tangential inertia force generated by swing were negligible. But the fluctuation of mass flow rate caused by swing motion affected the

hydrodynamic pressure force, drag force and shear lift force significantly, which would affect bubble sliding and detachment, and change the heat transfer near the heated wall eventually. The pressure drop under the swing conditions was larger than that under the motionless condition. The pressure drop of boiling flow fluctuated around that of the single phase flow, and the amplitude of fluctuation increased with the wall heat flux.

Mass transfer is one of the most significant parts of the numerical model. Schrage proposed a theory for evaporation at liquid-vapor interfaces in which the net mass flux across the interface is given by [31]

$$m'' = \frac{2\varepsilon}{2-\varepsilon}\sqrt{\frac{M}{2\pi R}}\left(\frac{P_{g\_lg}}{\sqrt{T_{g\_lg}}} - \frac{P_{sat}}{\sqrt{T_{lg}}}\right) \quad (1)$$

Eq. (1) is also called Hertz-Knudsen-Schrage Equation [32] or Kucherov-Rikenglaz Equation [32-34]. It is derived based on the Maxwell velocity distribution, the detailed derivation can be found in Dr. Carey's book [33] (page 135-140). Lee [35] further assumed the phase change occurs at a constant pressure and at a quasi thermo-equilibrium state. Under Lee's assumption, Clausius-Clapeyron equation can be applied to Hertz-Knudsen Equation to eliminate pressure and result in a new form which is mainly dependent of the saturation temperature and the relaxation time coefficient. It is stated in ANSYS FLUENT Theory Guide (on page 16-104) that the relaxation time coefficient needs to be tuned. An analysis of evaporation coefficient and condensation coefficient of water has been studied by Marek et al. [32]. They proved that evaporation and condensation coefficient of water obtained theoretically and experimentally rather scatter in a range of more than two decades with the condensation coefficient exceeding the evaporation coefficient, and both coefficients decrease with increasing temperature and increasing pressure,

whereas the relaxation time for both liquid and gas were adopted as 100 s^{-1} in Yang [28], Chen [29], and Wei's [30] work. Yang et al. pointed out that excessively large value of the relaxation time coefficient causes a numerical convergence problem, while too small values lead to a significant deviation between the interfacial temperature and the saturation temperature. Since the Clausius-Clapeyron equation was applied in the derivation of the mass source term, which requires a small temperature difference, large temperature deviation will invalid the accurateness of the mass source term. The value of both evaporation and condensation coefficient are adopted as 100 s^{-1} in this work. The reason for the value of the coefficients and relative derivation will be discussed in the part of mass transfer in Chapter 3.

Chapter 2 NUCLEATION STUDY

2.1 Types of nucleation

2.1.1 Homogeneous nucleation

Bubble nucleation completely within a superheated uniform liquid without any preferential nucleation sites is called homogeneous nucleation. The same term can also be used to describe droplet formation completely within supercooled vapor. Homogeneous nucleation occurs spontaneously and randomly, but it requires superheating of the medium. Compared to heterogeneous nucleation, homogeneous nucleation occurs with much more difficulty in the interior of a substance. Pure liquids that have been thoroughly degassed may still experience bubble formation at molecular vapor clusters within the bulk liquid.

2.1.2 Heterogeneous nucleation

Heterogeneous nucleation occurs much more often than homogeneous nucleation. Heterogeneous nucleation forms at preferential sites such as phase boundaries, surface of containers, impurities like dust, and minute bubbles, which are either from non-condensable gas or entrapped in micro cavities. At such preferential sites, the effective surface energy is lower, thus diminishes the free energy barrier and facilitating nucleation. Compared with homogeneous nucleation, heterogeneous nucleation is by far the common process at the low superheat due to the larger required superheat for homogeneous nucleation.

2.2 Nucleation analysis

Most of the time, since the temperature is highest at the solid surface, formation of a vapor embryo is most likely to occur at the solid-liquid interface, with one possibility of homogeneous nucleation within the liquid closest to the solid surface, and the alternative of formation of a vapor embryo as a heterogeneous nucleation process. The possibilities have been studied as flowing from both homogeneous and heterogeneous points of view.

Based on the assumption that the temperature and chemical potential in the two phases must be equal at equilibrium, using the Gibbs-Duhem equation, ideal gas law, and Young-Laplace equation, the radius of a stable bubble r_e has been derived as follows [33]

$$r_e = \frac{2\sigma}{P_{sat}(T_l)\, exp\left(\frac{v_l\left(P_l - P_{sat}(T_l)\right)}{RT_l}\right) - P_l} \tag{2}$$

where v_l is the inverse of density for liquid.

The pressure of liquid is atmospheric in this work, whereas the saturation pressure of liquid changes with the liquid temperature. By substituting a sequence of reliable data [33] into this equation, a curve has been plotted showing the radius changing with superheat of the liquid. It can be seen from the figure that when the superheat is small, the radius of a stable bubble is very large. Especially, if P_l equals to P_{sat}, the radius will be infinity, which means all the liquid will evaporate. Since the film thickness is small which is about micrometers, large bubble is impossible to be formed. Moreover, the reasonable radius in accordance with the film thickness requires high superheat.

On the other hand, the non-condensable gas and mini bubbles trapped in the micro-structure supply the preferential nucleation sites for the heterogeneous nucleation. Accordingly, water nearby the mini bubble embryo evaporate and lead to bubble growing.

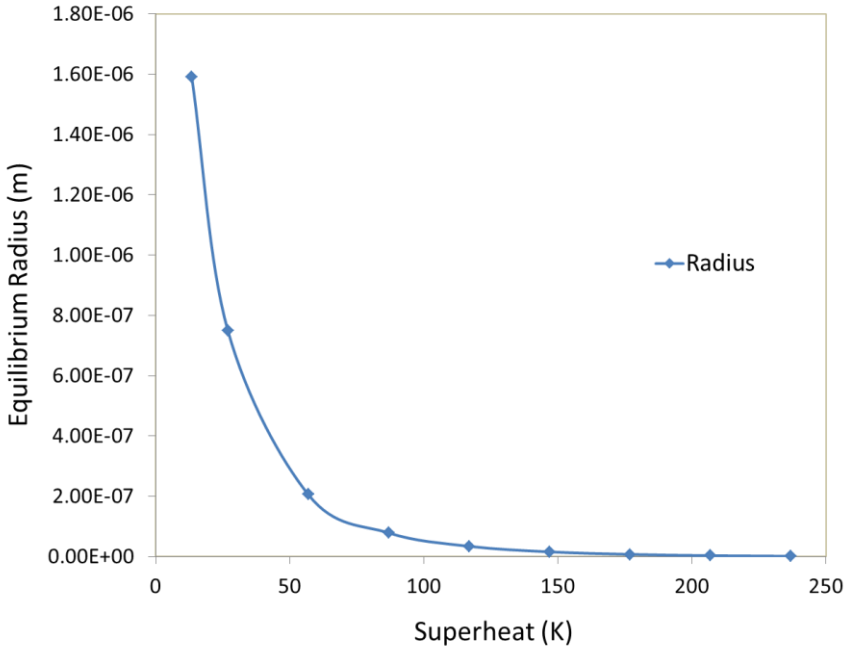

Fig. 1 Bubble equilibrium radius changes with superheat

Generally, since homogeneous nucleation requires a higher superheat than the heterogeneous nucleation, and the water pressure in this work is atmospheric pressure which confines the superheat, the nucleation sites in this work result from the non-condensable minute bubbles near the solid substrate.

Chapter 3 NUMERICAL MODELING

3.1 Computational domain and flooding scenario

The computational domain, composed of solid, liquid and gas parts, is shown in Fig. 2 as is the flooding scenario. The solid material and working fluid are aluminum and water, respectively. The length, width, and height are denoted by “L”, “W”, and “H”, respectively. The subscripts “s”, “l”, “g”, and “p” represent solid, liquid, gas, and pillar. “H”, without any subscript, is the height of the entire domain. The flooded condition requires $H_l > H_p$, which means the pillars are fully immersed by the working liquid. The four vertical boundaries in the 3-D domain are considered to be periodic in order to practically enable the limited computational domain to work as a horizontally extensive domain. A constant heat flux is given to the bottom surface of the solid as the heat source. In this work, we focus on the confined domain when the flooding condition occurs, thus the vapor which flows out of the computational domain is assumed to be removed quickly. Air with a constant temperature of 373.15 K is set at the outlet. Microstructures covered by four types of wettability patterns are done separately in this work, the geometry and wettability patterns are listed in Tab. 1.

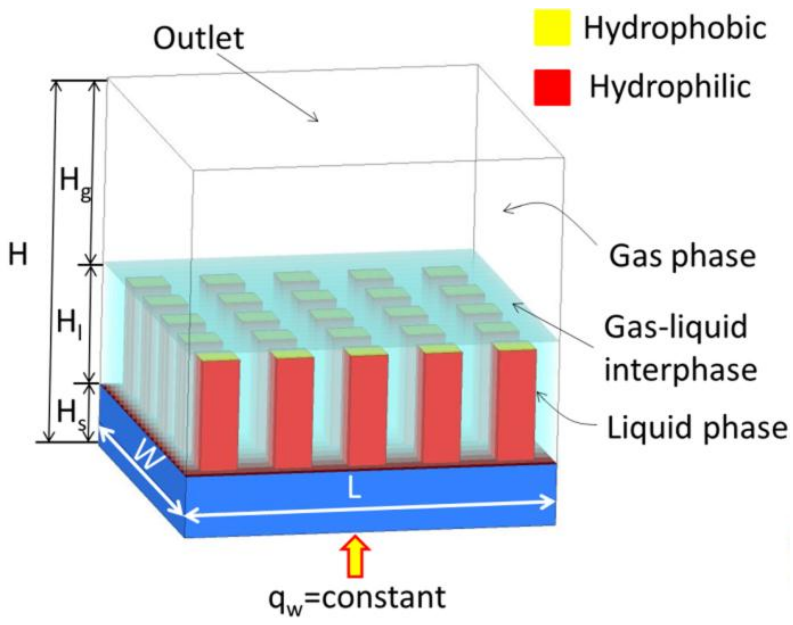

Fig. 2 Computational domain and flooding scenario

Tab. 1 Geometry details and wettability patterns of the simulation

Length unit: μm	H_s	H_l	H_g	W	L	Pillar size	Gap between two pillars	Pillar heights and wettability patterns
Structure effect on thermal performance	5	10	15	30	30	3 × 3	3	Pillar height for the hydrophilic flat surface: 0; Pillar heights for the hydrophobic patched cases: 0, 3, 5, 7, 9; The contact angles of hydrophilic and hydrophobic area are 5° and 108°, respectively.
Wettability pattern effect on bubble dynamic behavior	1	12	12	30	30	3 × 3	3	Pillar heights are 8 for all the four cases, wettability patterns are: 1. Wholly hydrophilic 2. Wettability gradient from 5° to 55° 3. Wettability gradient from 5° to 110° 4. Top patched with hydrophobic 110°

3.2 Governing equations

3.2.1 Volume of fluid method

The transient, three-dimensional Volume of Fluid (VOF) model is used, which has the capability of tracking the liquid-vapor interface and bubble trajectories continuously for the visualization of multi-bubble dynamics. A scalar field representing the portion of a phase volume occupation in a certain computational cell is defined as the phase volume fraction, which is denoted by α in this thesis. The liquid and gas phase volume fractions sum to unity,

$$\alpha_l + \alpha_g = 1 \tag{3}$$

The cell represents a liquid region if α_g= 0 and a gas region if α_g= 1. The relation 0 < α_g < 1 indicates that the cell contains both liquid and gas phases. The mixed properties for each cell, such as density, viscosity and thermal conductivity can be averaged by:

$$\rho = \alpha_l \rho_l + \alpha_g \rho_g \tag{4-1}$$

$$\mu = \alpha_l \mu_l + \alpha_g \mu_g \tag{4-2}$$

$$k = \alpha_l k_l + \alpha_g k_g \tag{4-3}$$

By introducing the phase volume fraction, the continuity equation, momentum equation, and energy equation can be modified. The tracking of the interfaces between the phases is accomplished by the solution of the continuity equations for the volume fraction of the phases:

$$\frac{\partial \alpha_l}{\partial t} + \nabla \cdot (\vec{v}\alpha_l) = \frac{\dot{m}_{g \to l}}{\rho_l} \tag{5-1}$$

$$\frac{\partial \alpha_g}{\partial t} + \nabla \cdot \left(\vec{v}\alpha_g\right) = \frac{\dot{m}_{l \to g}}{\rho_g} \tag{5-2}$$

where $\dot{m}_{g\to l}$ and $\dot{m}_{l\to g}$ are the source terms indicating the volumetric mass transfer rate due to phase change. How to define $\dot{m}_{g\to l}$ and $\dot{m}_{l\to g}$ will be discussed in section 3.3.

For the momentum equation shown as Eq. (6), it is solved throughout the domain, and the resulting velocity field is shared among the phases. The properties ρ and μ are dependent on the volume fractions of the phases. The gravity and the volumetric surface tension forces are taken into account. The volume based body force term F_{vol} is discussed in section 3.2.3.

$$\frac{\partial}{\partial t}(\rho\vec{v}) + \nabla\cdot(\rho\vec{v}\vec{v}) = -\nabla p + \nabla\cdot\left[\mu(\nabla\vec{v} + \nabla\vec{v}^{T}) - \frac{2}{3}\mu\nabla\cdot\vec{v}I\right] + \rho\vec{g} + F_{vol} \quad (6)$$

The energy equation, which is also shared among the phases, is written as

$$\frac{\partial}{\partial t}(\rho E) + \nabla\cdot\left(\vec{v}(\rho E + p)\right) = \nabla\cdot(k\nabla T) + Q \quad (7)$$

where $E = (\alpha_l\rho_l E_l + \alpha_g\rho_g E_g)/(\alpha_l\rho_l + \alpha_g\rho_g)$. E_l and E_g are based on the specific heat of their phases and shared temperature, respectively. The properties ρ and k are shared by phases, too. Q is the summation of the energy sources for the gas phase and liquid phase and any other volumetric heat sources which are zero here:

$$Q_{l\to g} = \dot{m}_{l\to g}h_{lg} \quad (8-1)$$

$$Q_{g\to l} = -\dot{m}_{l\to g}h_{lg} \quad (8-2)$$

3.2.2 **Interface Representation**

As it is mentioned in the former section, the interface is located in the cells which contain both phases, i.e., the phase volume fraction of the cells are in the frame of 0 to 1. To get a smooth interface and interpolate the face fluxes, the reconstruction based scheme: Geo-reconstruct is adopted in this work, which is the most accurate scheme in ANSYS FLUENT. To represent the interface between fluids, this scheme

applies a piecewise-linear approach to the cells that lie near the interphase between two phases. It assumes that the interface between two fluids has a linear slope within each cell, and uses this linear shape for calculation of the advection of fluid through the cell faces [36].

There are three steps in the reconstruction scheme: the first step is calculating the position of the linear interface relative to the center of each partially-filled cell, based on information about the volume fraction and its derivatives in the cell. The second step is calculating the advecting amount of fluid through each face using the computed linear interface representation and information about the normal and tangential velocity distribution on the face. The third step is calculating the volume fraction in each cell using the balance of fluxes calculated during the previous step.

3.2.3 **Surface tension**

Surface tension is a force arises as a result of attractive forces between molecules in a fluid. It acts to balance the radially inward intermolecular attractive force and the radially outward pressure gradient force across the surface.

The surface tension model in this work is the Continuum Surface Force (CSF) model, which was proposed by Brackbill et al. [37] for cells containing the gas-liquid interface. With this model, the surface tension results in a source term in the momentum equation in the VOF calculation.

Consider the Young-Laplace equation which shows that the pressure drop across the surface depends on the surface tension coefficient σ, and the surface curvature as measured by two radii, R_1 and R_2, in orthogonal direction:

$$p_g - p_l = \sigma\left(\frac{1}{R_1} + \frac{1}{R_2}\right) \tag{9}$$

where the pressure p_g and p_l are the pressure on either side of the liquid-gas interface.

In the CSF model, the surface curvature is computed from local gradient in the surface normal at the interface. The surface normal $\vec{n}$ can be defined as the gradient of α in the relative phase.

$$\vec{n} = \nabla\alpha \tag{10}$$

The curvature is defined in terms of the divergence of the unit normal

$$\kappa = \nabla \cdot \hat{n} \tag{11}$$

where

$$\hat{n} = \frac{\vec{n}}{|n|} \tag{12}$$

The surface tension can be written in term of the pressure jump across the surface. By using the divergence theorem, the force at the surface can be expressed as a volume force, acting as a source term in the momentum equation with the following form:

$$F_{vol} = \sigma \frac{\alpha_l \rho_l \kappa_g \nabla\alpha_g + \alpha_g \rho_g \kappa_l \nabla\alpha_l}{\frac{1}{2}(\rho_l + \rho_g)} \tag{13}$$

Since only two phases are present in a cell in this work, $\kappa_l = -\kappa_g$, and $\nabla\alpha_l = \nabla\alpha_g$, then Eq. (13) simplifies to

$$F_{vol} = \sigma \frac{\rho \kappa_g \nabla\alpha_g}{\frac{1}{2}(\rho_l + \rho_g)} \tag{14}$$

or

$$F_{vol} = \sigma \frac{\rho \kappa_l \nabla\alpha_l}{\frac{1}{2}(\rho_l + \rho_g)} \tag{15}$$

where ρ is the volume averaged density using Eq. (4-1).

3.2.4 **Wall adhesion**

The model used in this work to specify a wall adhesion angle in conjunction with the surface tension model is taken from Brackbill's work [37]. Instead of imposing the boundary condition at the wall itself, the contact angle is used to adjust the surface normal in cells near the wall. The according result of the so called dynamic boundary condition is the adjustment of the curvature of the surface near the wall. If θ_w is the contact angle, then the surface normal at the live cell next to the wall is

$$\hat{n} = \hat{n}_w cos\theta_w + \hat{t}_w sin\theta_w \tag{16}$$

where $\hat{n}_w$ and $\hat{t}_w$ are the unit vectors normal and tangential to the wall, respectively.

The local curvature of the surface is determined by the combination of this contact angle and the normally calculated surface normal one cell away from the wall. The body force term is adjusted accordingly by the obtained curvature to implement the surface tension calculation.

3.3 Mass transfer model

3.3.1 **Net mass flux**

Eq. (17), which is referred to as Hertz-Knudsen-Schrage Equation [32] or Kucherov-Rikenglaz Equation [32-34], is frequently used to calculate the net mass flux over the vapor/gas-liquid interface in a two-phase system. This equation, which is derived from the kinetic theory based on the Maxwell velocity distribution, can be expressed as

$$m'' = \beta \sqrt{\frac{M}{2\pi R}} \left(\frac{p_g}{\sqrt{T_g}} - \frac{p_l}{\sqrt{T_l}} \right) \tag{17}$$

in which the subscriptions "g" and "l" represent gas and liquid phases. Eq. (17) can also be written as Eq. (1), which deems the liquid-gas interface saturated and the gas temperature and pressure is measured in the gas phase near the liquid-gas interface.

β can be expressed as

$$\beta = \frac{2\varepsilon}{2-\varepsilon} \tag{18}$$

The ε is derived from the vaporization coefficient ε_e and the condensation coefficient ε_c. ε_e is defined as the portion of liquid molecules going to the vapor/gas side due to vaporization . The remaining fraction $1-\varepsilon_e$ is due to the "reflection" of vapor molecules that strike the interface but do not condense. The fraction ε_c is the fraction of molecules crossing the surface towards liquid that condense and are not "reflected". Usually ε_e and ε_c are assumed to be equal, although the validity of this assumption is suspect [33]. As a result, $\varepsilon_e = \varepsilon_c = \varepsilon$, where ε is often referred to as vaporization, evaporation, condensation, or accommodation coefficient.

Assuming the interface temperature to be equal to the vapor temperature near the interface [38, 39], Eq. (1) becomes

$$m'' = \beta \sqrt{\frac{M}{2\pi R T_{sat}}} \left(p_{g\_lg} - p_{sat}\right) \tag{19}$$

The Clapeyron-Clausius equation as shown in Eq. (20) relates the pressure to the temperature for the saturation condition.

$$\frac{dp}{dT} = \frac{h_{lg}}{T\left(v_g - v_l\right)} \tag{20}$$

v_g and v_l are the inverse of the density for the gas and liquid, respectively. h_{lg} is the latent heat. Based on the Clapeyron-Clausius equation, the variation of temperature can be obtained from variation of pressure close to the saturation temperature.

$$p_{g\_lg} - p_{sat} = \frac{h_{lg}}{T\left(v_g - v_l\right)}\left(T_{g\_lg} - T_{sat}\right) \tag{21}$$

Using this relation in Eq. (19) yields [40]

$$m'' = \beta\sqrt{\frac{M}{2\pi R T_{sat}}}\left(\frac{h_{lg}}{\frac{1}{\rho_g} - \frac{1}{\rho_l}}\right)\frac{T_{g\_lg} - T_{sat}}{T_{sat}} \tag{22}$$

3.3.2 **Mass source term**

In order to get the surface-volume rate to transfer Eq. (22) to a source term, the Sauter Mean Diameter (SMD) is introduced [41]. The SMD is typically defined in terms of the surface diameter, d_s:

$$d_s = \sqrt{\frac{A_p}{\pi}} \tag{23}$$

and the volume diameter, d_v

$$d_v = \left(\frac{6V_p}{\pi}\right)^{\frac{1}{3}} \tag{24}$$

The subscription "p" denotes "particle". A_{cell} and V_{cell} are the corresponding surface area and volume of the particle, respectively. If the the d_s and d_v are measured directly by other means without knowledge of A_p or V_p, SMD for a given cell is defined by

$$D_{sm} = \frac{{d_v}^3}{{d_s}^2} \tag{25}$$

If the actually surface area and volume of the cell are known, A_p divided by V_p can be simplified further

$$\frac{A_p}{V_p} = \frac{4\pi(d_s/2)^2}{(4/3)\pi(d_v/2)^3} = \frac{6}{D_{sm}} \tag{26}$$

It is assumed in FLUENT that all vapor bubbles have the same diameter, then the surface-volume rate can be estimated by the D_{sm} of the bubbles. Considering the definition of the phase volume fraction α, we have

$$V_p = \alpha V_{cell} \tag{27}$$

Substitute it back into Eq. (26), yields

$$\frac{A_p}{V_{cell}} = \frac{6\alpha}{D_{sm}} \tag{28}$$

Then the mass flux over the liquid vapor interface can be transformed into volume based mass source terms:

$$\dot{m} = m'' \frac{A_p}{V_{cell}} = \frac{6\alpha\beta}{D_{sm}} \sqrt{\frac{M}{2\pi R T_{sat}}} \left(\frac{h_{lg}\rho_l\rho_g}{\rho_l - \rho_g} \right) \frac{T_{g\_lg} - T_{sat}}{T_{sat}} \tag{29}$$

where A_p and V_{cell} are the bubble surface area and cell volume, respectively.

3.3.3 **Relaxation time coefficient**

The mass transport in this simulation is implemented using the evaporation-condensation mechanistic model proposed by Lee [35] in 1979. This model primarily concerns phase change at a quasi thermo-equilibrium state, and depends on the temperature difference between local temperature and saturation temperature. If local temperature is higher than the saturation temperature, the evaporation and boiling occurs, liquid water mass is transferred to a water vapor species of gas phase. Otherwise condensation will take place.

The relaxation time coefficients, which are represented by C_l and C_g in this article, were introduced in Lee's model:

$$C_l = \frac{6\beta}{D_{sm}} \sqrt{\frac{M}{2\pi R T_{sat}}} \frac{\rho_v h_{lg}}{\rho_l - \rho_g} \tag{30-1}$$

$$C_g = \frac{6\beta}{D_{sm}}\sqrt{\frac{M}{2\pi R T_{sat}}}\frac{\rho_l h_{lg}}{\rho_l - \rho_g} \qquad (30-2)$$

Considering the mass transfer direction and applying Eq. (30) in Eq. (29), the mass transfer can be simplified and described based on different temperature regimes as follows

$$\dot{m}_{l\to g} = \begin{cases} C_l \cdot \dfrac{\alpha_l \rho_l (T_l - T_{sat})}{T_{sat}} & T_l > T_{sat} \\ 0 & T_l \le T_{sat} \end{cases} \qquad (31-1)$$

$$\dot{m}_{g\to l} = \begin{cases} 0 & T_g \ge T_{sat} \\ C_g \cdot \dfrac{\alpha_g \rho_g (T_{sat} - T_g)}{T_{sat}} & T_g < T_{sat} \end{cases} \qquad (31-2)$$

where $\dot{m}$ (kg/m^3-s) is the mass transfer rate between two phases and is regarded as the source term in the continuity equation and energy equation; α and ρ are the phase volume fraction and density, respectively. Thus, the source term in the energy equation can be obtained by multiplying the mass transfer rate by the latent heat.

The mass transfer model described in Eq. (30-31), which was proposed by Lee, is implemented by FLUENT as the evaporation-condensation model. Since ε scatters in a range of more than two decades [32], as well as D_{sm} in Eq. (30) is difficult to determine, it is stated in FLUENT theory guide that the relaxation time coefficient needs to be fine tuned. Researchers [28-30] usually calibrate C_l and C_g using the experimental results. Yang et al.[28], Chen et al. [42], and Wei et al. [30] used a value of 100 s^{-1} for both C_l and C_g in their studies. Since there are not any experimental results reported on this problem, and the value does not affect the trend of the results which has been proved by the simulations, we use 100 s^{-1} in this work.

3.4 Species transport model

The species transport equation has the general form:

$$\frac{\partial}{\partial t}(\rho Y_i) + \nabla \cdot (\rho \vec{v} Y_i) = -\nabla \cdot \vec{J_\iota} + R_i + S_i \quad (32)$$

in which Y_i is the local mass fraction of the ith species, R_i is the net rate of production of species i by chemical reaction, and S_i is the rate of creation by addition from the dispersed phase plus any user-defined sources. $\vec{J_\iota}$ is the diffusion flux of species i, which arises due to gradient of concentration and temperature. The Fick's law is used to model the mass diffusion in this work, the temperature gradient is ignored, under which the diffusion flux can be written as:

$$\vec{J_\iota} = -\rho D_i \nabla Y_i \quad (33)$$

Here D_i is the mass diffusion coefficient for species i in the mixture.

Eq. (32) needs to be tuned to solve the conservation equation for chemical species in multiphase flows. For each phase k, the local mass fraction of each species, Y_i^k, can be predicted through the solution of a convection-diffusion equation for the ith species. Eq. (32) can be represented in the flowing form when applied to the current case, which includes two species: water vapor and air in the gas phase, and ignores the terms *R* and *S*.

$$\frac{\partial}{\partial t}(\rho^g \alpha^g Y_v{}^g) + \nabla \cdot (\rho^g \alpha^g \vec{v}^g Y_v{}^g) = \nabla \cdot \left(\rho^g \alpha^g D_{v,air} \nabla Y_v{}^g\right) + \left(\dot{m}_{l\to g} - \dot{m}_{g\to l}\right) \quad (34)$$

in which α^g is the volume fraction of the gas phase, $Y_v{}^g$ is the mass fraction of the vapor in the gas phase, $D_{v,air}$ is a constant mass diffusion coefficient between species of water vapor and air at saturation temperature, $\dot{m}$ is a source term due to the mass transfer between water vapor in gas phase and liquid phase.

3.5 Numerical simulation information

3.5.1 Numerical simulation method

The numerical solutions are obtained with the pressure-based finite volume scheme using the commercial CFD software ANSYS 14.5 FLUENT. The terms in the momentum, mass and energy equations are discretized using the second-order upwind differencing scheme. Pressure-velocity coupling is achieved using the SIMPLE algorithm. The geometric reconstruction interpolation scheme [43] is used for interface calculations. The time step, ranging between 1×10^{-9} s and 5×10^{-8} s, is variable to ensure the Courant number is smaller than 2. A mesh independent study has been made and shown in Section 3.5.2. In this work, a medium grid with a smallest cell size of 0.375 μm and cell number of 322,812 is used, with 8 mesh layers along the pillar's side.

3.5.2 Mesh independent study

To ensure the simulation results correct, the mesh independent study has been done with different cell numbers as 95, 316 for a coarse mesh, 322, 812 for a medium mesh, 635, 016 for a fine mesh. The mesh overview is shown in Fig. 3, in which the left column demonstrates the grid of the whole domain, and the right column illustrates the mesh layers of the pillars by hiding the water and vapor zones.

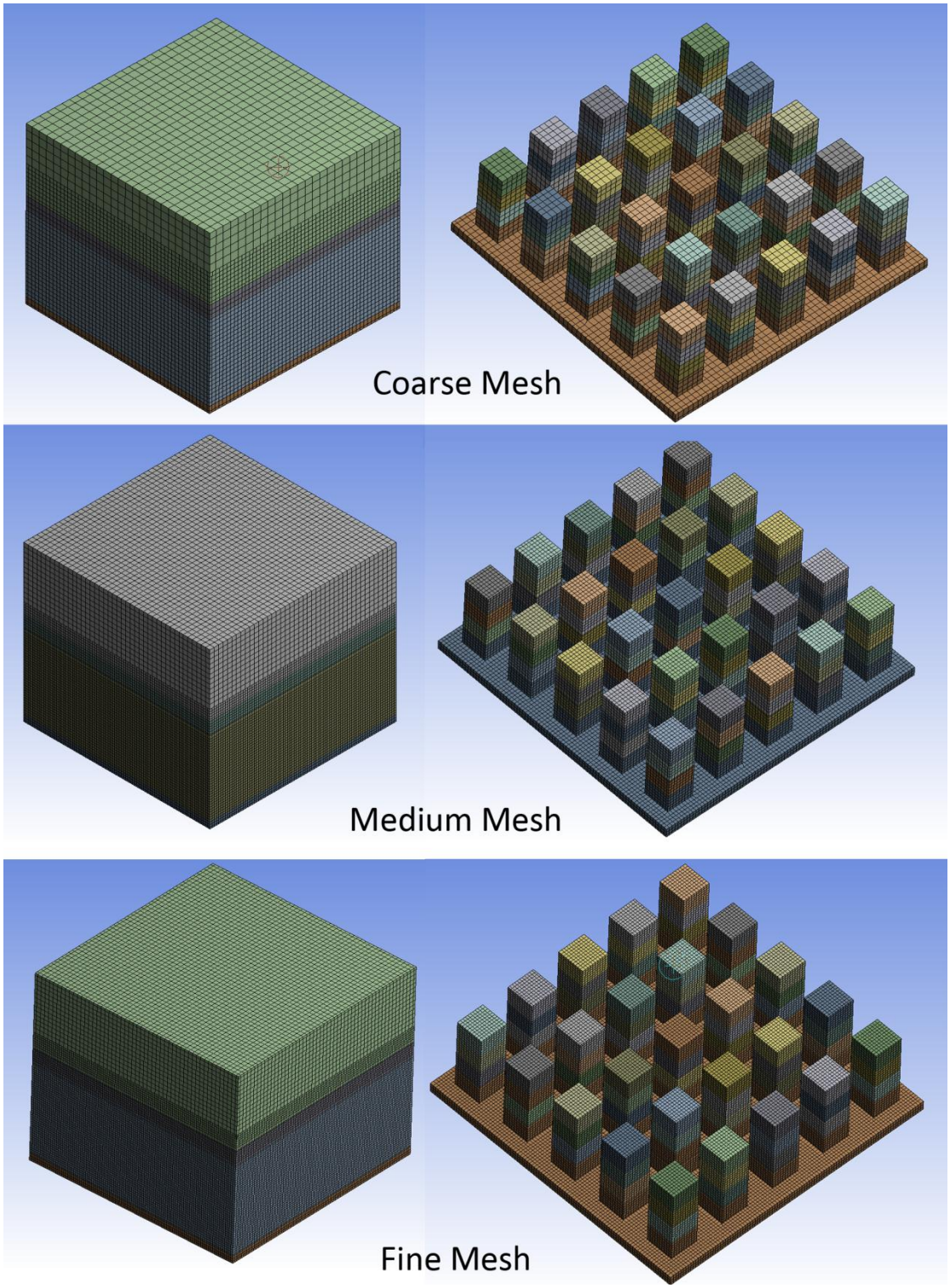

Fig. 3 Mesh overview

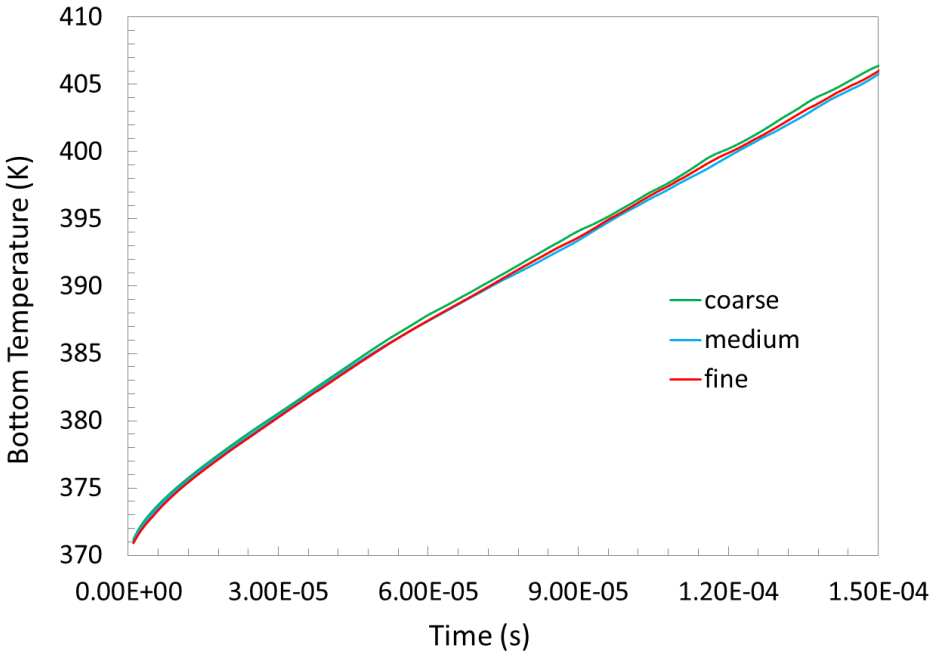

Fig. 4 Bottom temperature for different meshes

Fig. 4 demonstrates the bottom temperature changing with time. It can be seen that the curve for the coarse mesh deviates from the curves for the medium and fine meshes. Since the bottom temperature is not quite sensitive to the mesh, the bubble dynamics for different meshes has been looked into to further assist choosing an appropriate mesh. As it is shown in Fig. 5, bubbles are sparse in the course mesh, which is distinct from that in the medium and fine meshes. It can be noticed that bubbles do not exist when the time is 0.04 ms, whereas bubble embryos start to form in the other two meshes at the same time. Additionally, bubble distribution and density for the medium and fine meshes are more similar compared to that in the coarse mesh.

Based on the consideration of the bottom temperature and the bubble dynamics behavior, as well as the shorter computation time, the medium mesh is chosen for all the cases.

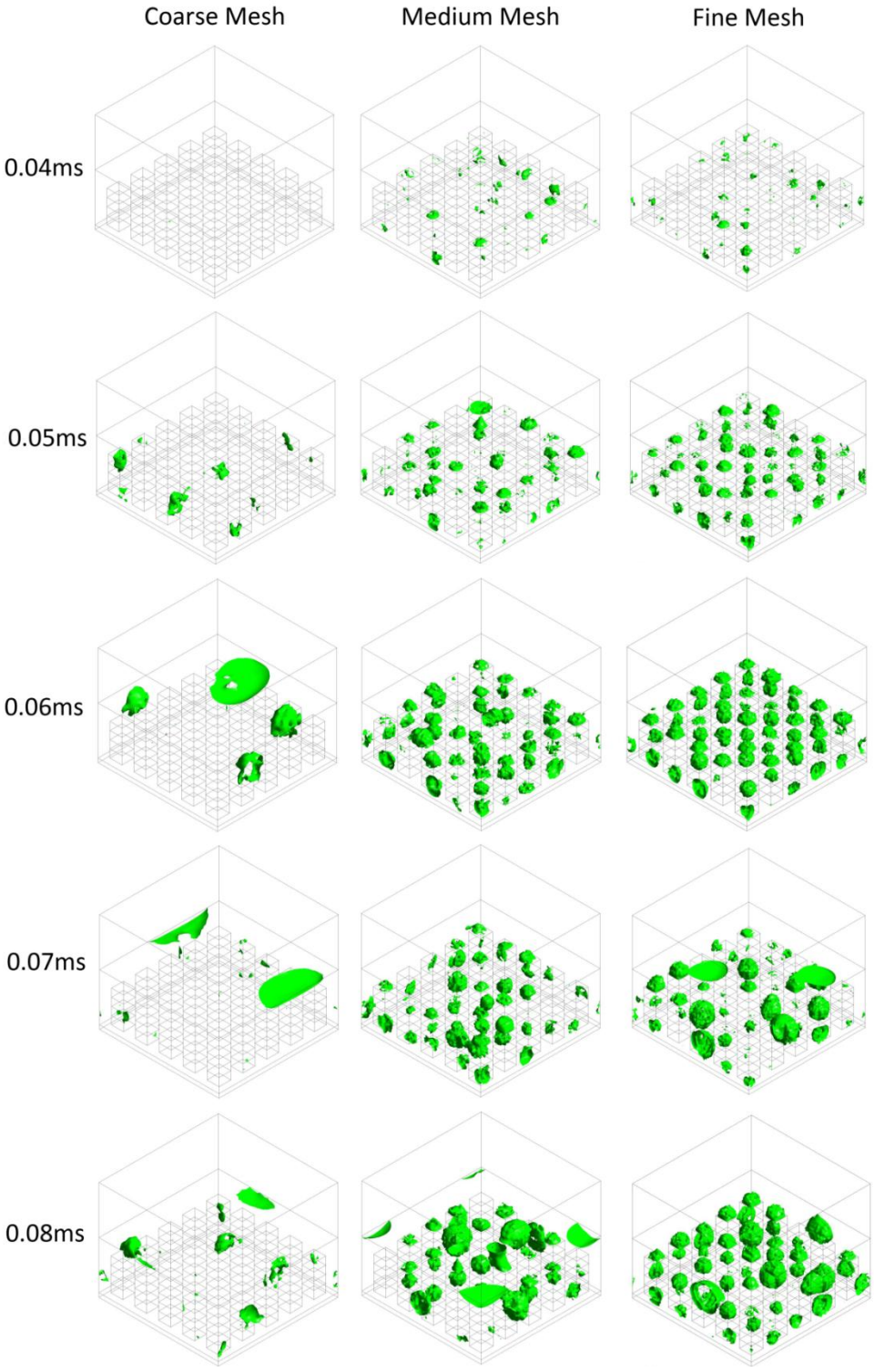

Fig. 5 Bubble evolution for different meshes

Chapter 4 Results and discussion

4.1 Structure effect and thermal performance

To investigate the pillar height's effect on the thermal performance of the micro-structures, we examine pillar height ranges from 3 μm to 9 μm, and utilize both a hydrophilic flat surface and a patterned flat surface. The dimensions of the computational domain are H = 30 μm, L = 30 μm and W= 30 μm. The thickness, H_s, of the solid substrate is 5 μm. The liquid film thickness, H_l, is set to be 10 μm to ensure the flooding condition. The remaining space is occupied by a vapor-air mixture, with the height H_g = 15 μm. A constant heat flux of 700 W/cm^2 is given to the bottom surface. The corresponding initial temperature for the whole domain is set to 370 K. The pillar array arrangement is set as 5 by 5, and the pillar cross-sectional area is designed as 3 μm by 3 μm, correspondingly. The contact angle of the hydrophilic substrate is set to be 5°, and 108° for the hydrophobic surface. The outlet of the computational domain, located on the top of the computational domain, is defined as a pressure outlet to allow free access for the gas phase mixture containing species of both water vapor and air. The backflow gas species is defined as dry air at a temperature of 370 K. The initial species of gas phase is defined as dry air. Fig. 6 displays the configurations of the micro-structures with different pillar heights and a wholly hydrophilic flat surface.

It is easy to see in Fig. 7 that the flat surface with the wettability patterns has the lowest heat transfer coefficient, rather than the hydrophilic flat surface. The hydrophilic flat surface has a 25.6% higher value than the one with wettability patterns, of which the corresponding value is 251 kW/m^2 K. This could be attributed

to the fact that the bubbles prefer to adhere on the hydrophobic spots, and thus form a partial dry-out scenario and attenuate the heat dissipation.

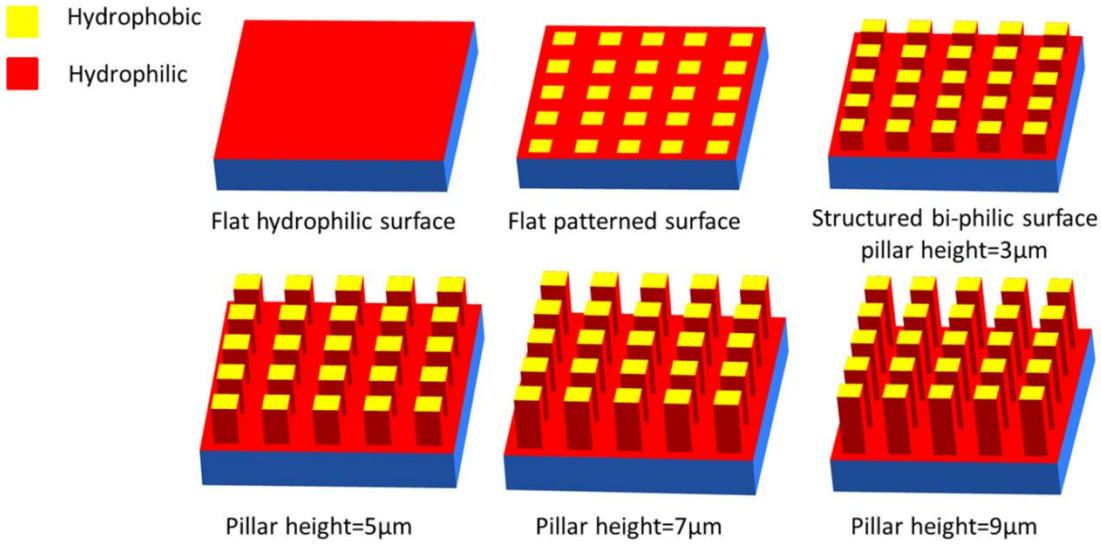

Fig. 6 Configurations of series with different pillar heights

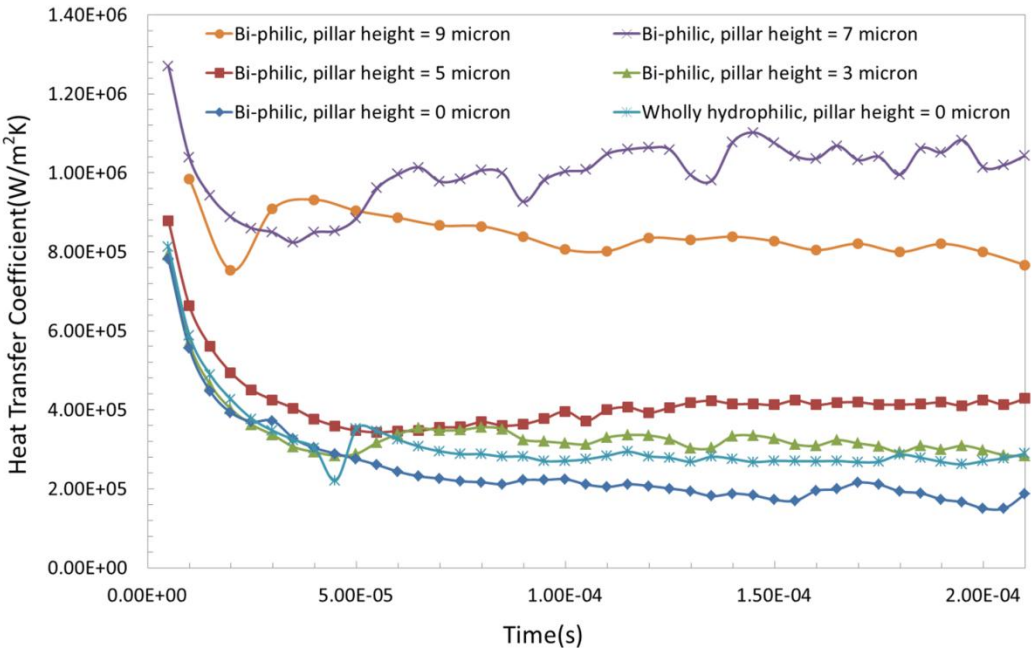

Fig. 7 Heat transfer coefficients of different micro-structures

The heat transfer enhancement by the structured surface can also be recognized. The time averaged heat transfer coefficient of structured surfaces with 3 μm, 5 μm, 7 μm and 9 μm pillars are 8.4%, 33.2%, 217.7%, and 167.1% higher than the

hydrophilic flat surface, respectively.. Because of the excellent thermal dissipation from solid to liquid, relatively smaller temperature gaps between the solid and liquid can be achieved, thus, the heat transfer coefficient of the structured surfaces with 7 μm and 9 μm pillars are significantly higher than the others, revealing excellent heat dissipation capacity. However, the averaged heat transfer coefficient does not increase monotonously with the growth of pillar height. The most remarkable heat transfer coefficient is obtained from the structure with 7 μm, instead of the 9 μm pillar structure.

It can be observed from Fig. 8 that it is easier for the 9 μm pillar to expose the top surface to the gas phase, since the hydrophobic substance prefers gas to water. Therefore, the liquid-gas interface is pinned on the top edges of the pillars due to too many exposures, the contact area between the liquid and solid is reduced, and consequently the thermal performance is weakened. From this point of view, a critical value of pillar height exists for a liquid film of certain thickness. The resulting heat transfer performance is determined by a tradeoff between the solid surface area improvement and the "sticking" phenomenon at the hydrophobic pillar tops.

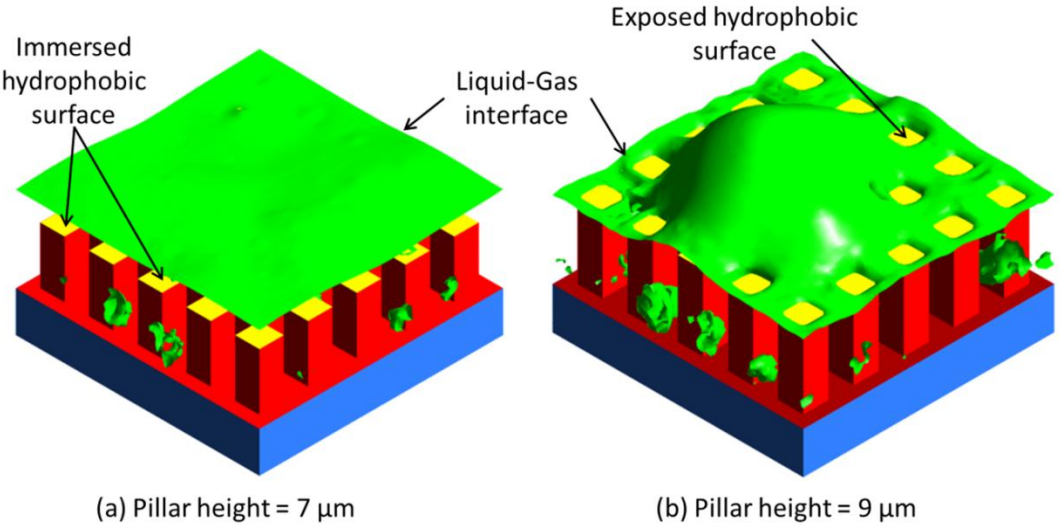

Fig. 8 Liquid-gas interface pins at the top edges of the pillars

4.2 Effect of wettability pattern on bubble dynamic behavior

Considering that the thickness of the solid substrate will not affect the comparison result, and in order to reduce the simulation time, H_s in this series of cases is reduced to 1 μm. The dimensions of the computational domain are H = 25 μm, L = 30 μm and W = 30 μm. All micro-pillars are set as high as 8 μm, while the liquid depth H_l = 12 μm to ensure flooding. The remaining space was occupied by a vapor/air mixture, with height H_g = 12 μm. A constant heat flux of 1 kW/cm^2 is given to the bottom surface. There are four types of wettability patterns studied in this series of cases in order to investigate their effect on bubble dynamic behavior and thermal performance. Fig. 9 displays detailed information about contact angle distribution. The side of the pillar, which is covered by a wettability gradient texture, is divided into four parts uniformly; each part is 2 μm high. Other settings are the same as that of the former cases, including initial temperature for the whole domain, the pillar's length and array, etc.

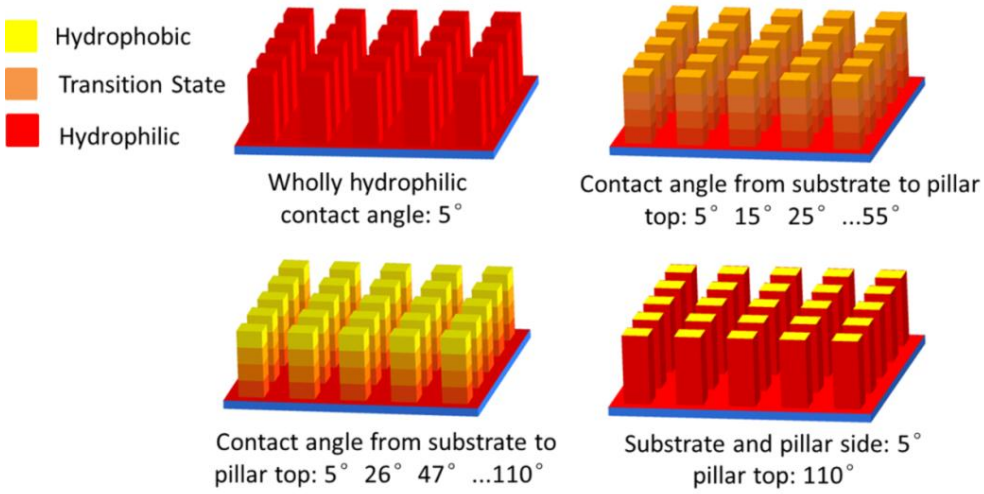

Fig. 9 Configurations of series with different wettability patterns

Four columns of images, as shown in Fig. 10, demonstrate bubble's evolution on four kinds of micro-structures with the same time interval and starting point, which is 0.04 ms, since bubbles start to form then.

When compared with the bubbles in the wholly hydrophilic micro-structure, bubbles within the pillars, which are patterned by the wettability gradient from contact angles of 5° to 55°, move faster in the upward direction. Fig. 11 illuminates the difference in detail. The velocity field comparison is demonstrated in Fig. 12 at the time of 0.058 ms. It can be seen from Figs. 11 and 12 that the micro-structure patterned with the wettability gradient can promote the bubble's upward velocity.

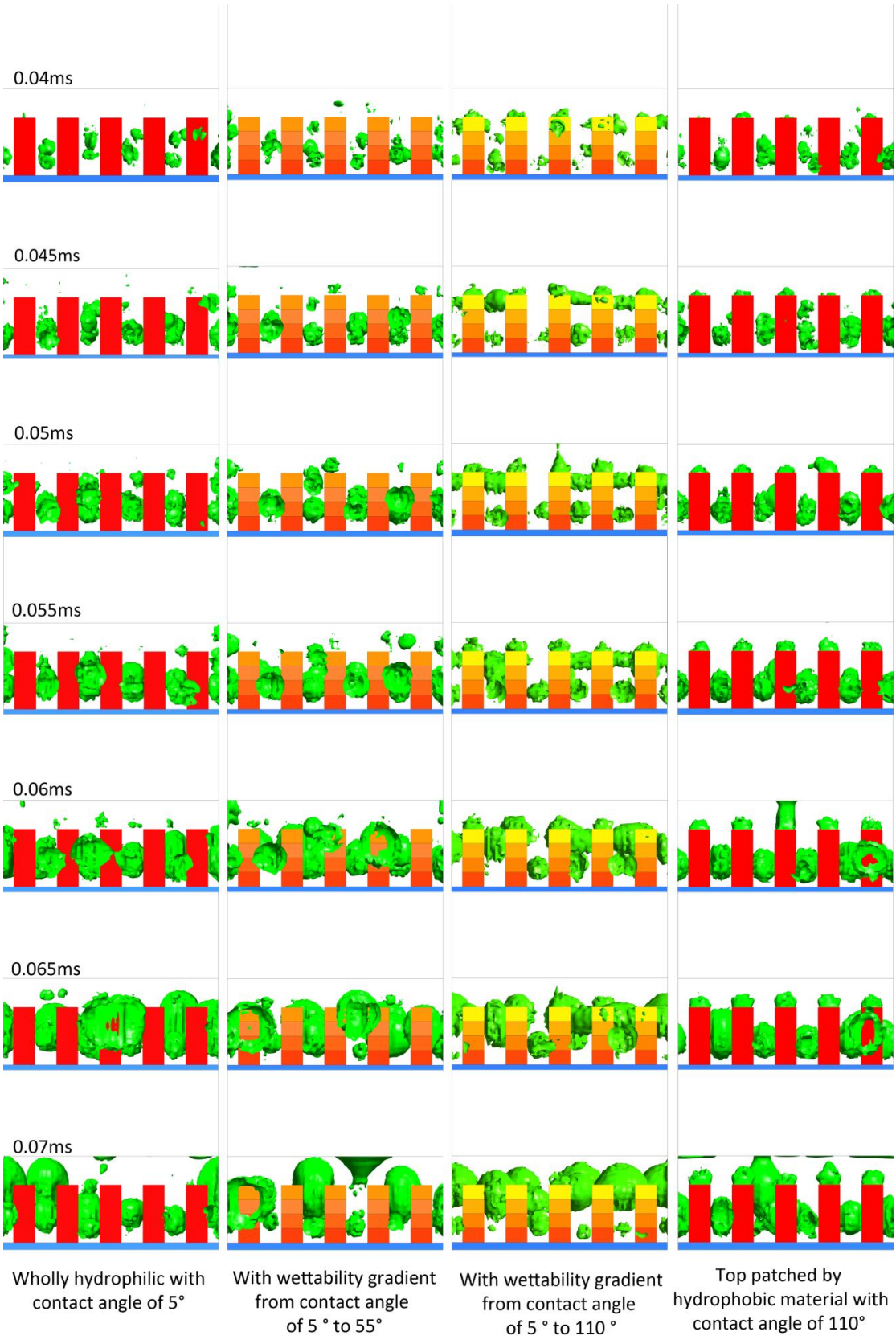

Fig. 10 Bubble evolution on four kinds of micro-structures

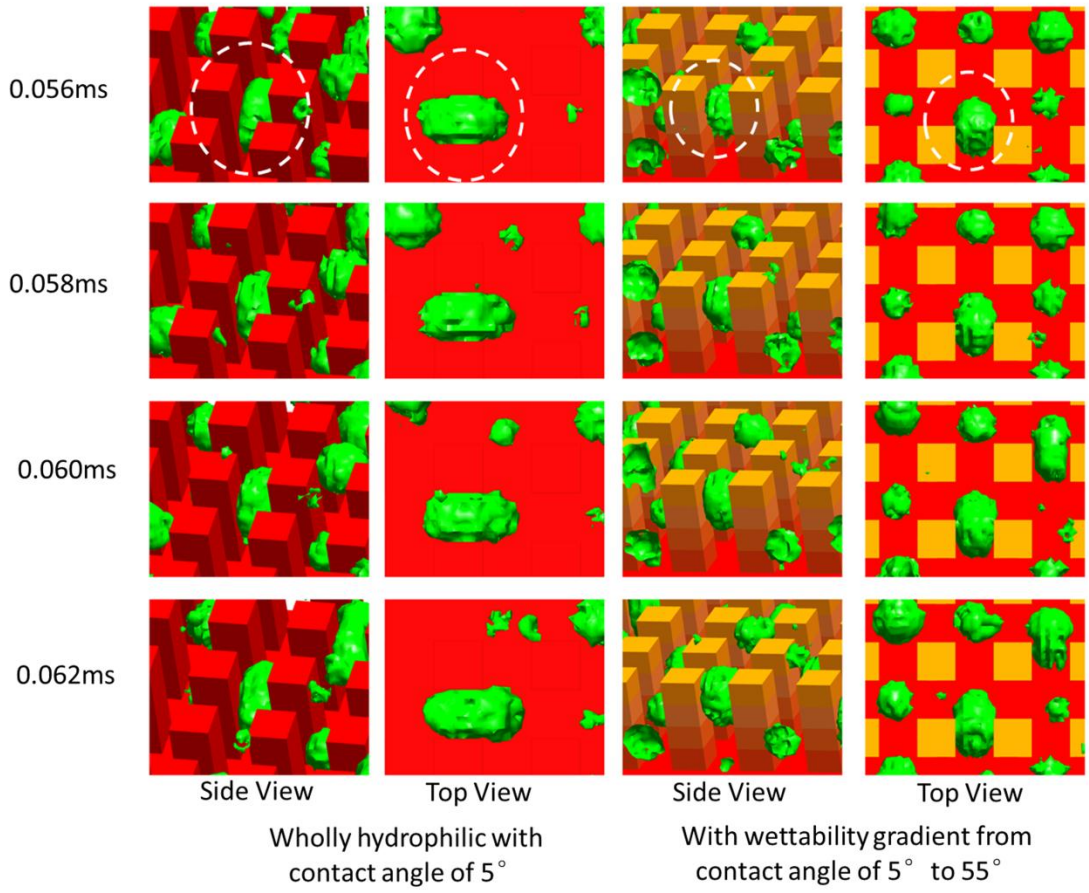

Fig. 11 Comparison of bubble upward velocity between micro-structures with wholly hydrophilic and wettability gradient patterns

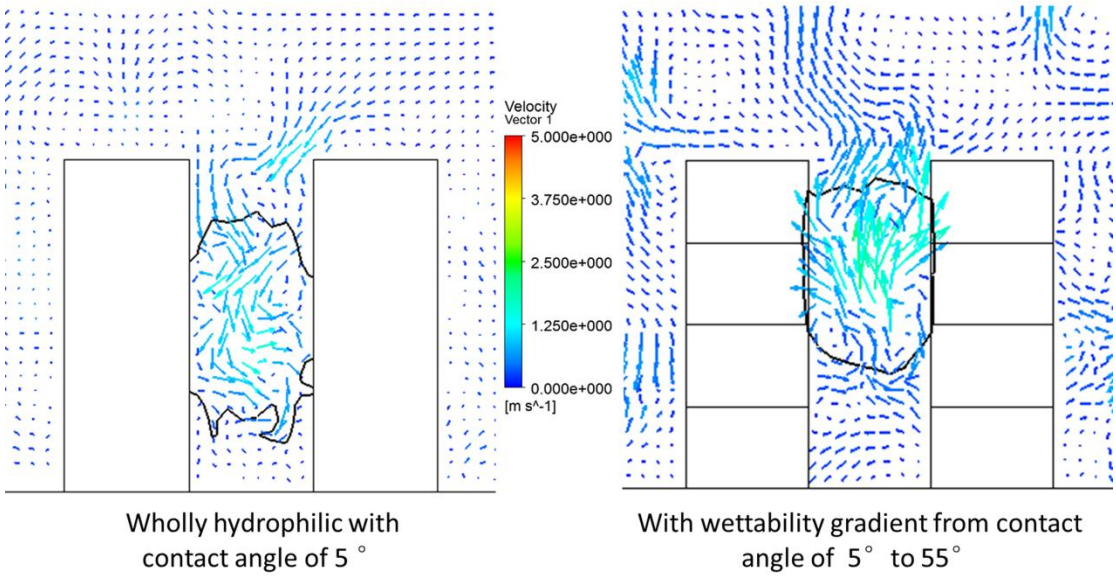

Fig. 12 Comparison of velocity field between micro-structures with wholly hydrophilic and wettability gradient patterns at 0.058 ms

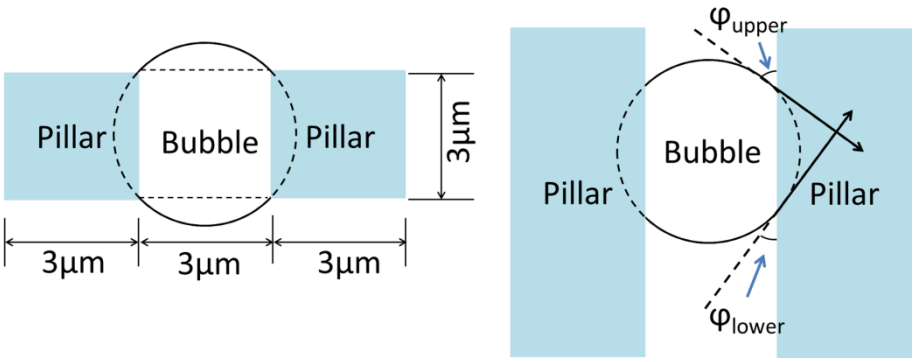

Fig. 13 Sketch of surface tension force analysis

This phenomenon results from the difference of the surface tension's vertical component, which is between the upper and lower contact interfaces of the bubble and pillar. The force analysis is done as follows. According to the dimensions of the micro-structure, if a bubble occupies the place between two abreast pillars and contacts both of them as Fig. 13 specifies, its volume can be calculated as 35.3 μm^3. On one hand, the buoyancy force imposed on the bubble will be 3.46×10^{-13} N; On the other hand, the vertical component of surface tension force can be calculated by:

$$\begin{aligned} F_{stf} &= 2\times\left(\int(\sigma cos\varphi_{upper}dl)sin\theta+\int(\sigma cos\varphi_{lower}dl)sin\theta\right) \\ &= 2\times\left(\int_0^{180}\sigma r cos\varphi_{upper}sin\theta d\theta+\int_{180}^{360}\sigma r cos\varphi_{lower}sin\theta d\theta\right) \\ &= 4\sigma r\left(cos\varphi_{upper}-cos\varphi_{lower}\right) \end{aligned} \tag{35}$$

in which the subscript "stf" means "surface tension force", "r" denotes the radius of the bubble. The pulling force F_{stf} will be 3.05×10^{-8} N, 3.92×10^{-8} N, 1.08×10^{-7} N, and 1.25×10^{-7} N, if φ_{upper} and φ_{lower} adopt values of 25° and 35°, 35° and 45°, 47° and 68°, 68° and 89°, respectively. It can be observed that the buoyancy force imposed on the bubble is several orders smaller than the surface tension force in the upwards direction, which means the pillars patched with the wettability gradient can supply a larger pulling force than the wholly hydrophilic one, within which the bubbles move toward the liquid-gas interface only by volume increase. Additionally,

the pulling force gets larger when the contact angle gradient increases, or when the bubble moves to a higher level, where the contact angle gets bigger.

Compared with the first three columns in Fig. 10, the top patched pillars in the fourth column promote bubble departure, while the other three cases have bubble pinning at the top of the pillar forest. The reasons for the pinning effect are various regarding different cases.

For the wholly hydrophilic micro-pillars, bubbles grow on their own or merge with other bubbles. Restrained by momentum conservation, bubbles in this case have no net upward movement, except the gradually enlarged volume, which can help bubbles to touch the water-gas interface and then depart. Before reaching the water-gas interface, bubbles stay pinned at the hydrophilic pillar tops.

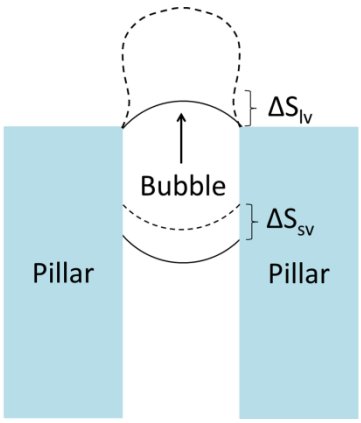

Fig. 14 Imaginary movement of a bubble pinning between two pillars

For the other two cases, which have wettability gradient patterns, although the gradient can promote bubble's upward movement, it still has difficulty in pushing the bubbles out from the pillars completely, due to the lack of sufficient pulling force or energy. Fig. 14 demonstrates an imaginary movement of a bubble pinning between two pillars, which have a hydrophilic contact angle gradient from 5° to 55°. If 35° is adopted as the contact angle of the surface ΔS_{sv}, the surface tension of this area can be calculated by [33]:

$$\sigma_{sv} - \sigma_{lv} - \sigma_{sl} = -\sigma_{lv}(1 - cos\varphi_{lower}) \quad (36-1)$$

$$\sigma_{sl} = \sigma_{lv} + \sigma_{sv} - 2(\sigma_{lv}\sigma_{sv})^{\frac{1}{2}} \quad (36-2)$$

in which the water surface tension is 0.0589 N/m at a temperature of 373.15K. The results are σ_{sv} = 0.0487 N/m and σ_{sl} = 0.00048 N/m. If the movement specified by the dashed line occurs, the increased energy, or the required extra work, can be specified as:

$$W_{pull} = \Delta S_{lv}\sigma_{lv} + \Delta S_{sl}\sigma_{sl} - \Delta S_{sv}\sigma_{sv} \quad (37)$$

where the letter "S" denotes an area with units of m^2. Considering that $\Delta S_{sl} = \Delta S_{sv} \approx \Delta S_{lv}$, the expression can be rewritten as

$$W_{pull} = \Delta S_{sl}(\sigma_{lv} + \sigma_{sl} - \sigma_{sv}) \quad (38)$$

Presuming the bubble moves upward by 1 μm, the increased energy can be calculated as 6.41×10^{-14} J.

However, no matter if the pulling force is valued as 3.05×10^{-8} N or 3.92×10^{-8} N, the energy released during the process is much smaller than required, which means the imaginary movement will not happen, and the pinning effect will take place.

When it comes to the pillars with a hydrophobic gradient pattern, i.e., from the contact angle of 5° to 110°, the same thing will happen due to the lack of energy supply. The difference between the two types of pinning that occur in the second and third columns in Fig. 10 is that bubbles in the third case are supper-large and cover the entire tip of the pillars, resulting in a vapor blanket which greatly decreases the heat transfer coefficient.

Bubble departure is realized in two steps: growth and vertical movement, and contact with the water-gas interface. Once a bubble reaches the water surface it will escape from the water quickly, due to the water surface tension and the high pressure inside the bubble. However, the first three kinds of micro-structures, as shown in Fig.

10, have the same problem, which is that bubbles pin at the pillar tops, and the only way to expel the bubbles for the three cases is to allow the bubbles to grow until the bubble size is large enough to reach the water surface. Although the second and third micro-structures can promote vertical movement of the bubble, the assistance disappears when bubbles reach the top of the pillar forest. This type of departure, depending on the bubble's isotropic expanding, is inefficient, whereas pillars patched by hydrophobic material on the pillar tops, as shown in the fourth column in Fig. 10, can dramatically promote the escape of bubbles. The pulling effect from the pinned bubble is displayed in Fig. 15. It can be observed that the bubble can be easily pulled up and completely escape with the help of the bubbles sitting on the pillar tops, whereas the bubble in the micro-structure with the wettability gradient pattern has no

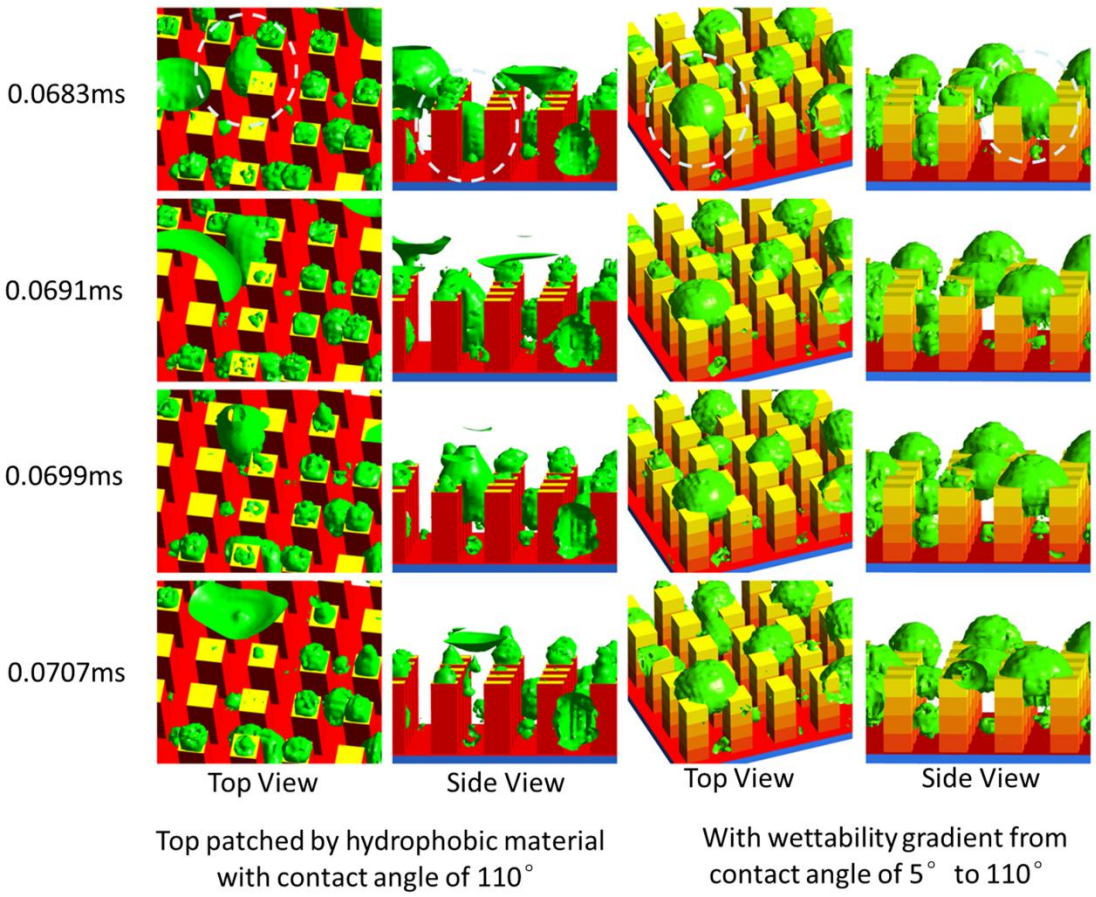

Fig. 15 Pulling effect of sit-on-top bubble

obvious change at the same time.

From Fig. 12 it can be seen that the surface appears serrated. This is caused by four factors: first, there are phase changes which happen near the surface continuously throughout time, and new born small bubbles merge with the large bubble, causing the unsmooth surface; second, the reaction is fast and severe, such that the surface tension has no time to achieve a smooth surface; third, the mesh is relatively course when the

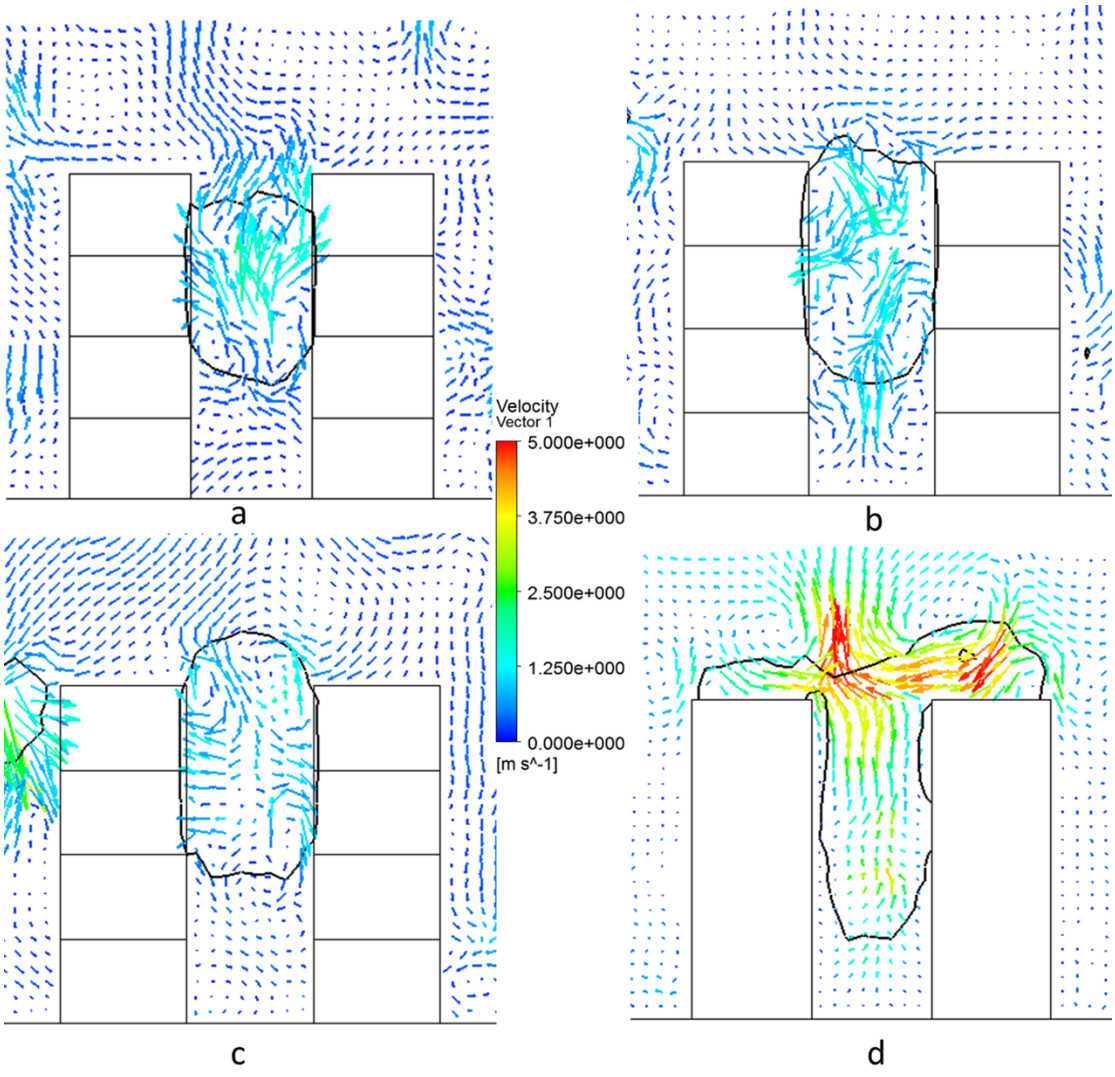

Fig. 16 Evolution and comparison of velocity field between micro-structures with wettability gradient patterns and hydrophobic patch on pillar tops. a, b, c: with wettability gradient from contact angle of 5 °to 55 °, flow time are 0.058ms, 0.064ms, and 0.070ms, respectively; d: top patched by hydrophobic material with contact angle of 110 °

bubble is small; fourth, the 2-d cutting plane of the complex, 3-D, multiple bubble interaction could make the interface look more uneven.

Fig. 16a to Fig. 16c demonstrate that the pulling assistance disappeared after the bubble reached the pillar's top level. Additionally, compared with Fig. 16d, it can be seen that the upwards velocity of the case with the wettability gradient is smaller than that of the case patched by hydrophobic material on the pillar's top.

The promotion effect happens because the surface energy releases during the bubble merging, and the released energy transforms into kinetic energy which helps the bubble to contact the liquid-gas interface quickly. How the surface energy decreases after merging is explained as follows. For two bubbles' merging, assume the radii of the two small bubbles are r_a and r_b. r_{ab} denotes the radius of the merged bubble. Suppose the water vapor is ideal gas, which obeys

$$pV = nRT \tag{39}$$

Since the mole numbers of the merged bubble should be the same as the sum of the two small bubbles, it can be obtained that

$$\begin{aligned} p_{ab}V_{ab} &= n_{ab}RT \\ &= (n_a + n_b)RT \\ &= p_aV_a + p_bV_b \end{aligned} \tag{40}$$

The relation between water pressure and bubble's internal pressure can also be obtained from the Young-Laplace equation

$$p_{ab} = p_l + \frac{2\sigma}{r_{ab}} \tag{41}$$

If the two bubbles are identical, this yields

$$p_a = p_b = p_l + \frac{2\sigma}{r_a} \tag{42}$$

Substituting Eqs. (41) and (42), and the volume of the bubbles back into Eq. (40), yields

$$\frac{4}{3}\pi {r_{ab}}^3\left(p_l+\frac{2\sigma}{r_{ab}}\right)=2\left(p_l+\frac{2\sigma}{r_a}\right)\frac{4}{3}\pi {r_a}^3 \tag{43}$$

r_{ab} can be expressed by r_a in a very complicated polynomial from this equation. If r_a is evaluated as 2×10^{-6} m, the surface energy difference between the two small bubbles and the new large bubble can be calculated by

$$W_{merge}=\sigma(S_a+S_b-S_{ab}) \tag{44}$$

After substituting all of the values into Eq. (44), the value of W_{merge} can be obtained as $1.271\pi\sigma r a^2$. This means the bubble will do work to the ambient environment since the value is positive. This is easy to understand because substances in nature prefer to stay in the form which possesses the lowest energy, and the ball shape has the smallest surface area among all kinds of shapes with the same volume. The released energy can be transformed to help the lower bubble to climb up with the pillars' reaction force. If the vertical distance that the bubbles' center of gravity moves is deemed as 2 μm, the vertical, average pulling forth imposed upon the bubble could be estimated by

$$F_{merge}=\frac{W_{merge}}{s} \tag{45}$$

in which "s" denotes the moving distance. The average pulling force is approximately 4.7×10^{-7} N, calculated by Eq. (45). This is one order larger than the pulling force induced by the wettability gradient we got, which means the bubbles sitting on the pillars' top have a more effective effort than the wettability gradient. This result can also be validated in Fig. 16d.

It can be noticed in Fig. 10 that bubbles shown in the third and fourth column start to form on the pillar tip from a very early stage. These bubbles contribute to the

effort to pull up bubbles in the lower level. However, since pillars in the fourth column have a lower contact angle of 5° on the side, it is easier for bubbles to detach from the hydrophilic surface than from the hydrophobic one for the case in the third column, and avoid the pinning effect. This is another trade-off between the large bubble pinning effect and the quick bubble expelling process.

4.3 Comparative studies for structure with different wettability patterns

Based on the results in Fig. 17, the structure patched by hydrophobic material on the top has the best thermal performance, since it has the lowest bottom temperature, while the curves for the other three cases coincide. Large bubbles pinning at the pillar tops might be the main reason leading to the poorer result. This can also be validated in Fig. 18, which displays the heat transfer coefficient curves.

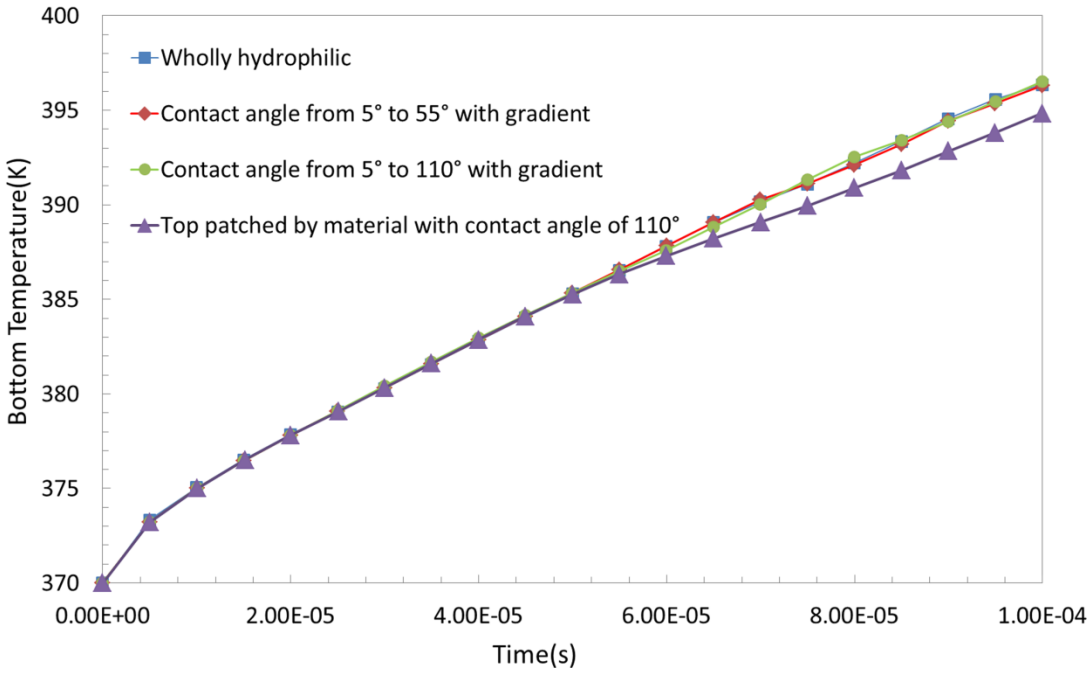

Fig. 17 Bottom surface temperatures for different wettability patterns

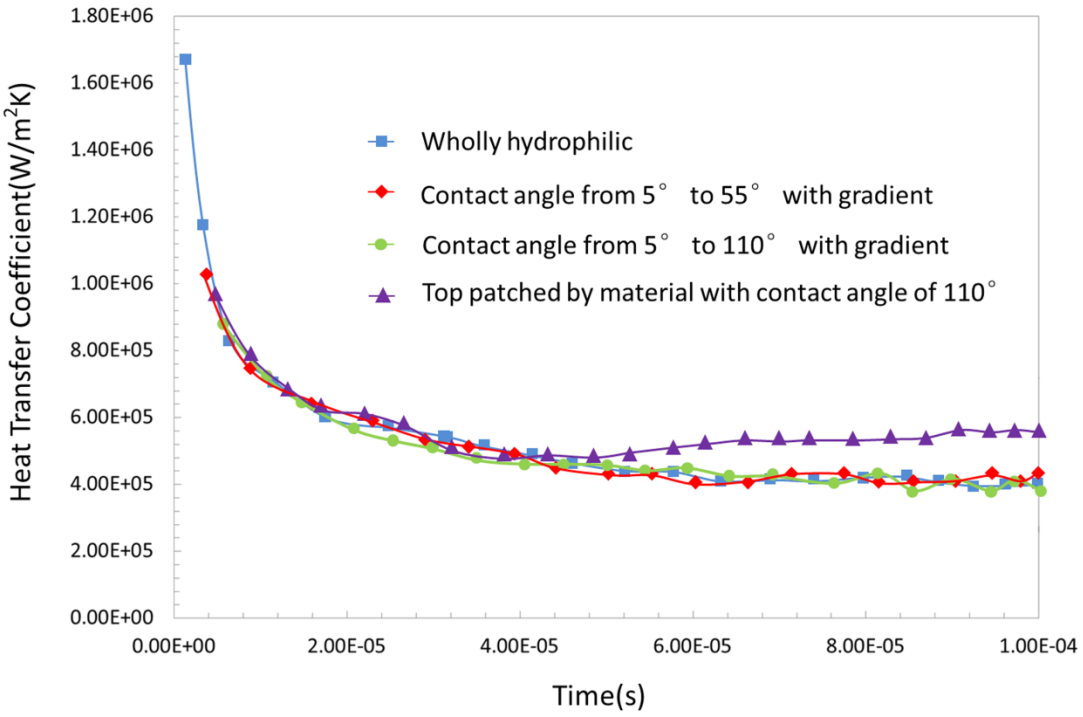

Fig. 18 Heat transfer coefficients on surfaces with different wettability patterns

Chapter 5 Conclusions

A transient 3-D Volume of Fluid model is used to investigate two phase cooling on enhanced surfaces, which combines micro-pillars and different engineered wettability patterns under flooding conditions. The simulation results shows that the heat dissipation performance is improved with an increase in pillar height, since a higher pillar enables liquid water to be heated faster and more uniformly. However, the heat transfer coefficient is not monotonously improved, due to the pinning effect on the pillar's top edges. For the micro-structures patched with wettability gradient patterns on the pillar sides, although the bubble's upward movement can be promoted, which can be seen from the visualized dynamics, insufficient pulling force and energy results in large bubble pinning at the pillar tops, which forms a vapor blanket which consequently decreases the heat transfer coefficient. However, for the pillars that have hydrophobic material patched on the top, due to the favorable effect of hydrophobic surfaces on vapor accumulation, bubbles can be formed on the pillar tops, which can provide an effective pulling force to help more bubbles to depart from the pillar forest. The pulling force is supplied by the surface energy released during the bubble merging process. The simulation results, including heat source temperatures and heat transfer coefficients, prove that only a patch of hydrophobic material on the pillar top works best out of all of the cases.

Future work will focus on investigating refined micro-structures which can deal with the trade-off between the large bubble pinning effect and the quick bubble expelling process. Study over the micro-structure at different levels of dry-out will also be performed.

Reference

[1] Bar-Cohen, A., Wang, P., and Rahim, E., 2007, "Thermal management of high heat flux nanoelectronic chips," Microgravity Sci. Technol, 19(3-4), pp. 48-52.

[2] Bar-Cohen, A., and Wang, P., 2012, "Thermal Management of On-Chip Hot Spot," Journal of Heat Transfer, 134(5), pp. 051017-051017.

[3] Sabry, M. N., 2005, "Compact thermal models for internal convection," Components and Packaging Technologies, IEEE Transactions on, 28(1), pp. 58-64.

[4] Park, K. A., and Bergles, A. E., "Boiling heat transfer characteristics of simulated microelectronic chips with detachable heat sinks," Proc. International Heat Transfer Conference, p. 4.

[5] Honda, H., Wei, J. J., and Takamastu, H., 2001, "Enhanced Boiling of FC-72 on Silicon Chips With Micro-Pin-Fins and Submicron-Scale Roughness," Journal of Heat Transfer, 124(2), pp. 383-390.

[6] Bowers, M. B., and Mudawar, I., 1994, "High flux boiling in low flow rate, low pressure drop mini-channel and micro-channel heat sinks," International Journal of Heat and Mass Transfer, 37(2), pp. 321-332.

[7] Knight, R. W., Hall, D. J., Goodling, J. S., and Jaeger, R. C., 1992, "Heat sink optimization with application to microchannels," Components, Hybrids, and Manufacturing Technology, IEEE Transactions on, 15(5), pp. 832-842.

[8] Wadsworth, D. C., and Mudawar, I., 1992, "Enhancement of Single-Phase Heat Transfer and Critical Heat Flux From an Ultra-High-Flux Simulated Microelectronic Heat Source to a Rectangular Impinging Jet of Dielectric Liquid," Journal of Heat Transfer, 114(3), pp. 764-768.

[9] Estes, K. A., and Mudawar, I., 1995, "Comparison of Two-Phase Electronic Cooling Using Free Jets and Sprays," Journal of Electronic Packaging, 117(4), pp. 323-332.

[10] Hsieh, C.-C., and Yao, S.-C., 2006, "Evaporative heat transfer characteristics of a water spray on micro-structured silicon surfaces," International Journal of Heat and Mass Transfer, 49(5–6), pp. 962-974.

[11] Yang, J., Chow, L. C., and Pais, M. R., 1996, "Nucleate Boiling Heat Transfer in Spray Cooling," Journal of Heat Transfer, 118(3), pp. 668-671.

[12] Kim, J., 2007, "Spray cooling heat transfer: The state of the art," International Journal of Heat and Fluid Flow, 28(4), pp. 753-767.

[13] Horacek, B., Kiger, K. T., and Kim, J., 2005, "Single nozzle spray cooling heat transfer mechanisms," International Journal of Heat and Mass Transfer, 48(8), pp. 1425-1438.

[14] Bostanci, H., Rini, D. P., Kizito, J. P., Singh, V., Seal, S., and Chow, L. C., 2012, "High heat flux spray cooling with ammonia: Investigation of enhanced surfaces for CHF," International Journal of Heat and Mass Transfer, 55(13–14), pp. 3849-3856.

[15] Cheng, J. T., and Chen, C. L., 2010, "Active thermal management of on-chip hot spots using EWOD-driven droplet microfluidics," Exp Fluids, 49(6), pp. 1349-1357.

[16] Cheng, J. T., and Chen, C. L., 2010, "Adaptive Chip Cooling Using Electrowetting on Coplanar Control Electrodes," Nanoscale and Microscale Thermophysical Engineering, 14(2), pp. 63-74.

[17] Baird, E., and Mohseni, K., 2008, "Digitized Heat Transfer: A New Paradigm for Thermal Management of Compact Micro Systems," Components and Packaging Technologies, IEEE Transactions on, 31(1), pp. 143-151.

[18] Park, K. A., and Bergles, A. E., "Boiling heat transfer characteristics of simulated microelectronic chips with detachable heat sinks," Proc. Heat Transfer 1986, Proceedings of the Eighth International Heat Transfer Conference, Hemisphere Publ Corp, pp. 2099-2104.

[19] Tuckerman, D. B., and Pease, R. F. W., 1981, "High-performance heat sinking for VLSI," Electron Device Letters, IEEE, 2(5), pp. 126-129.

[20] Shen, J., Graber, C., Liburdy, J., Pence, D., and Narayanan, V., 2010, "Simultaneous droplet impingement dynamics and heat transfer on nano-structured surfaces," Experimental Thermal and Fluid Science, 34(4), pp. 496-503.

[21] Zhou, Z., Shi, J., Chen, H.-H., Schafer, S. R., and Chen, C.-L., 2014, "Two-phase flow over flooded micro-pillar structures with engineered wettability pattern," International Journal of Heat and Mass Transfer, 71(0), pp. 593-605.

[22] Wang, X., Zhao, S., Wang, H., and Pan, T., 2012, "Bubble formation on superhydrophobic-micropatterned copper surfaces," Applied Thermal Engineering, 35(0), pp. 112-119.

[23] Renkun, C., Ming-Chang, L., Vinod, S., Zhijie, W., Hyung Hee, C., and Arun, M., 2009, "Nanowires for Enhanced Boiling Heat Transfer," Nano Letters, 9(2), pp. 548-553.

[24] Cao, X. L., Cheng, P., and Zhao, T. S., 2002, "Experimental study of evaporative heat transfer in sintered copper bidispersed wick structures," Journal of Thermophysics and Heat Transfer, 16(4), pp. 547-552.

[25] ćoso, D., Srinivasan, V., Ming-Chang, L., Je-Young, C., and Majumdar, A., 2012, "Enhanced Heat Transfer in Biporous Wicks in the Thin Liquid Film Evaporation and Boiling Regimes," Journal of Heat Transfer, 134(10), pp. 1-11.

[26] Betz, A. R., Xu, J., Qiu, H., and Attinger, D., 2010, "Do surfaces with mixed hydrophilic and hydrophobic areas enhance pool boiling?," Applied Physics Letters, 97(14), p. 141909.

[27] Betz, A. R., Jenkins, J., Kim, C.-J. C., and Attinger, D., 2013, "Boiling heat transfer on superhydrophilic, superhydrophobic, and superbiphilic surfaces," International Journal of Heat & Mass Transfer, 57(2), pp. 733-741.

[28] Yang, Z., Peng, X. F., and Ye, P., 2008, "Numerical and experimental investigation of two phase flow during boiling in a coiled tube," International Journal of Heat and Mass Transfer, 51(5–6), pp. 1003-1016.

[29] Fang, C., David, M., Rogacs, A., and Goodson, K., 2010, "Volume of Fluid Simulation of Boiling Two-Phase Flow in a Vapor-Venting Microchannel," Frontiers in Heat and Mass Transfer, 1(1).

[30] Wei, J.-h., Pan, L.-m., Chen, D.-q., Zhang, H., Xu, J.-j., and Huang, Y.-p., 2011, "Numerical simulation of bubble behaviors in subcooled flow boiling under swing motion," Nuclear Engineering and Design, 241(8), pp. 2898-2908.

[31] Schrage, R. W., 1953, A Theoretical Study of Interface Mass Transfer, Columbia University Press, New York.

[32] Marek, R., and Straub, J., 2001, "Analysis of the evaporation coefficient and the condensation coefficient of water," International Journal of Heat and Mass Transfer, 44(1), pp. 39-53.

[33] Carey, V. P., 1992, Liquid-vapor Phase-change Phenomena, Hemisphere Publishing Corporation.

[34] Kucherov, R. Y., and Rikenglaz, L. E., 1960, "The problem of measuring the condensation coefficient," Doklady Akad Nauk SSSR, 133(5), pp. 1130-1131.

[35] Lee, W. H., 1980, A pressure iteration scheme for two-phase flow modeling, Hemisphere Publishing, Washington, DC.

[36] Youngs, D. L., 1982, "Time-dependent multi-material flow with large fluid distortion," Numerical methods for fluid dynamics, 24, pp. 273-285.

[37] Brackbill, J. U., Kothe, D. B., and Zemach, C., 1992, "A continuum method for modeling surface tension," Journal of Computational Physics, 100(2), pp. 335-354.

[38] Dhavaleswarapu, H. K., Murthy, J. Y., and Garimella, S. V., 2012, "Numerical investigation of an evaporating meniscus in a channel," International Journal of Heat and Mass Transfer, 55(4), pp. 915-924.

[39] Faghri, A., 1995, Heat Pipe Science and Technology, Taylor & Francis, Washington DC.

[40] Tanasawa, I., 1991, "Advances in Condensation Heat Transfer," Advances in Heat Transfer, T. F. I. James P. Hartnett, and I. C. Young, eds., Elsevier, pp. 55-139.

[41] Crowe, C. T., Schwarzkopf, J. D., Sommerfeld, M., and Tsuji, Y., 1998, Multiphase Flows with Droplets and Particles, CRC press.

[42] Chen, F., Milnes, D., Anita, R., and Kenneth, G., 2010, "Volume of fluid simulation of boiling two-phase flow in a vapor-venting microchannel," Heat Mass Transfer, 1(1).

[43] Youngs, D., 1982, "Time-dependent multi-material flow with large fluid distortion," Numerical methods for fluid dynamics, 24, pp. 273-285.